

A crystal symmetry-invariant Kobayashi–Warren–Carter grain boundary model and its implementation using a thresholding algorithm

Jaekwang Kim^a, Matt Jacobs^b, Stanley Osher^b, Nikhil Chandra Admal^{a,*}

^a*Department of Mechanical Science and Engineering, University of Illinois Urbana–Champaign*

^b*Department of Mathematics, University of California Los Angeles*

Abstract

One of the most important aims of grain boundary modeling is to predict the evolution of a large collection of grains in phenomena such as abnormal grain growth, coupled grain boundary motion, and recrystallization that occur under extreme thermomechanical loads. A unified framework to study the coevolution of grain boundaries with bulk plasticity has recently been developed by [Admal et al. \(2018\)](#), which is based on modeling grain boundaries as continuum dislocations governed by an energy based on the Kobayashi–Warren–Carter (KWC) model ([Kobayashi et al., 1998, 2000](#)). While the resulting unified model demonstrates coupled grain boundary motion and polygonization (seen in recrystallization), it is restricted to grain boundary energies of the Read–Shockley type, which applies only to small misorientation angles. In addition, the implementation of the unified model using finite elements inherits the computational challenges of the KWC model that originate from the singular diffusive nature of its governing equations. The main goal of this study is to generalize the KWC functional to grain boundary energies beyond the Read–Shockley-type that respect the bicrystallography of grain boundaries. The computational challenges of the KWC model are addressed by developing a thresholding method that relies on a primal dual algorithm and the fast marching method, resulting in an $\mathcal{O}(N \log N)$ algorithm, where N is the number of grid points. We validate the model by demonstrating the Herring angle and the von Neumann–Mullins relations, followed by a study of the grain microstructure evolution in a two-dimensional face-centered cubic copper polycrystal with crystal symmetry-invariant grain boundary energy data obtained from the covariance grain boundary model of [Runnels et al. \(2016a,b\)](#).

Keywords: A. phase field model, microstructures, B. motion by curvature, constitutive behavior, polycrystalline materials

*Corresponding author

Email address: admal@illinois.edu (Nikhil Chandra Admal)

1. Introduction

Most metals and ceramics exist as polycrystals, which are aggregates of single crystal grains stacked together along grain boundaries. The microstructure of a polycrystal is often characterized by the orientation distribution of its grains commonly referred to as texture. The macroscopic properties of polycrystals, which include yield strength, resistance to creep, fatigue, thermal and magnetic properties, are strongly influenced by texture. Grain boundary engineering refers to the strategy of enhancing the properties of polycrystalline materials by transforming the grain boundary character distribution to a desired state using thermo-mechanical processes (Watanabe, 2011). Mapping the microstructure-property relationship, and modeling the evolution of microstructure under various manufacturing processes are fundamental open problems relevant to grain boundary engineering.

The evolution of grain boundaries is driven by a long list of thermodynamic forces, of which surface tension plays a central role. For instance, grain boundaries in the isotropic Mullins’ model (Mullins, 1956) are driven by their excess surface energy resulting in motion by curvature with velocity given by

$$v = -m\gamma\kappa, \tag{1.1}$$

where κ and γ denote curvature and misorientation-dependent energy density of the grain boundary respectively, while m represents a constant mobility. More generally, an anisotropic grain boundary evolution arises from the dependence of m and γ on the grain boundary character defined by the five macroscopic degrees of freedom, which represent the misorientation and the inclination of the grain boundary.¹ Recent advances in the development of accurate interatomic potentials have enabled us to build and refine the grain boundary energy and mobility landscapes as functions of the grain boundary character (Chen et al., 2020; Runnels et al., 2016a,b; Olmsted et al., 2009; Bulatov et al., 2013). The grain boundary energy landscape reflects the symmetry of a bicrystal, and understanding the role of crystal symmetry contributes enormously towards characterizing grain microstructure evolution. Moreover, precisely identifying the grain boundary character distribution responsible for phenomena such as abnormal grain growth and recrystallization remains an open problem in materials science. This motivates us to undertake simulations of large ensembles of appropriately sampled polycrystals to discover lower-order statistical models for grain microstructure evolution. *The goal of this paper is to develop a lightweight model for motion by curvature in the presence of a misorientation-dependent grain boundary energy density, that can be implemented using an ultrafast algorithm.*

While motion by curvature is the simplest description of grain boundary evolution, experiments (Rollett, 2018; Barmak et al., 2013) and atomistic simulations (Upmanyu et al., 1998; Janssens et al., 2006) demonstrate that surface tension alone is not the dominant force. Molecular dynamics (MD) simulations have revealed that as grain boundaries evolve, they plastically deform the underlying material resulting in lattice distortions that give rise to additional forces on the grain boundary. In order to include the effect of grain boundary plasticity, recent mesoscale models (Admal et al., 2018) have focused on the coevolution grain boundaries and deformation. Evidently, such models subsume motion by curvature as

¹Under an anisotropic energy density γ that depends on the inclination n of a grain boundary, (1.1) transforms as $v = -m\kappa(\gamma + \partial^2\gamma/\partial n^2)$.

a special case, and are computationally more expensive, which is another motivation for us to seek an ultrafast algorithm. While the focus of this paper is motion by curvature, we ensure that our model is amenable to generalizations that include grain boundary plasticity.

Models for grain microstructure evolution can be broadly classified into three categories: probabilistic, diffuse-interface, and sharp-interface models. An example of a probabilistic grain growth model is the Monte-Carlo Potts model (Anderson et al., 1958, 1989; Mendeleev and Srolovitz, 2002; Upmanyu et al., 2002; Yang et al., 2000), wherein a polycrystal is described using points in a lattice, which are allocated to different grains. A grain boundary is implicitly defined by adjacent lattice points that belong to different grains. Evolution of the microstructure is carried out stochastically through random jumps of boundaries in thermodynamically favorable directions. While the advantage of the Monte-Carlo Potts model lies in the simplicity of its implementation, it relies on heuristic rules that do not have a thermodynamic basis.

In sharp interface models (Mullins, 1956; Hillert, 1965; Allen and Cahn, 1979), grain boundaries are modeled as surfaces that evolve according to motion by curvature given in (1.1). Methods to implement (1.1) rely on either implicitly or explicitly tracking the moving grain boundaries. For instance, front tracking methods (Frost et al., 1990, 1988; Kinderlehrer et al., 2004, 2006) describe grain boundaries in two dimensions as line segments along with their connectivity. Such a description breaks down at critical events including disappearance of shrinking grains and topological changes due to merging of grain boundaries. Therefore, front tracking methods are supplied with additional rules to redefine the connectivity of line segments to describe such critical events. The level set method (Zhao et al., 1996; Fausty et al., 2018) addresses the above limitation using an implicit representation. Each grain is described by a function that is positive within, and negative outside the grain, which implies the zero-valued isosurface describes the interface surrounding the grain. An implicit representation can describe topological changes without any additional rules. Yet, the main disadvantage of the level set method is that it does not extend to handle surfaces with self intersection and junctions, which occur in polycrystals. More recently, a thresholding method commonly referred to as the Merriman–Bence–Osher (MBO) (Merriman et al., 1992) scheme and its generalization by Esedoğlu and Otto (2015) have been shown to simulate grain kinetics very efficiently in addition to its ability to predict grain nucleation. The level set and the MBO methods are memory intensive as they use as many functions as the number of grains in order to describe a polycrystal. For example, a description of a 3D polycrystal with 10,000 grains on a $256 \times 256 \times 256$ grid requires ~ 1 TB of memory. Thus, for a large scale simulation, an additional numerical technique is devised to employ a level set function that approximates a large subset of spatially separated grains (Elsey et al., 2009, 2011). The thresholding method of Esedoğlu and Otto (2015), which is first-order accurate in time, has recently been extended by Zaitzeff et al. (2020) to a second-order method that is unconditionally energy stable. In general, all sharp-interface models can be incorporated with misorientation dependent grain boundary energy densities and mobilities. However, including inclination dependence is more challenging, and recent works by Basak and Gupta (2014); Hallberg and Bulatov (2019); Joshi et al. (2020) have addressed this challenge.

In diffuse interface models (Jokisaari et al., 2017), a polycrystal is defined using functions called phase fields, which are constant in the interior of the grains. The regions where the gradients of phase fields are non-zero are identified as diffused grain boundaries, which have a

characteristic width. A numerical implementation of a diffuse interface model requires a grid that is refined enough to resolve the width of the grain boundary. Therefore, diffuse interface models are computationally more expensive than their sharp-interface counterparts such as the level set and MBO methods. The *multi phase field* (MPF) model (Chen, 2002; Hirouchi et al., 2012; Steinbach, 2009), and the Kobayashi–Warren–Carter (KWC) model (Kobayashi et al., 1998, 2000; Warren et al., 2003) are two examples of diffuse-interface models for grain boundaries.

The main advantage of the MPF model lies in the simplicity of its construction to include misorientation dependent grain boundary energies and mobilities. Similar to the level set and the MBO methods, a naive implementation of the MPF method would use as many phase fields as the number of grains, resulting in an excessive use of computational memory. Since, at any point in the domain, only a few order parameters would be non-zero, recent implementations (Fan et al., 2002; Permann et al., 2016) of the MPF model allow multiple grains which do not share a common boundary to share the same order parameter. A *grain remapping* algorithm is used to strategically remap an order parameter shared by two distant grains when they approach close to each other. Recent advances (Ribot et al., 2019; Moelans et al., 2008; Kim et al., 2014) in MPF models explore the full anisotropy of grain boundary energy which consists of misorientation and inclination dependence.²

In contrast, the KWC model describes a two-dimensional polycrystal using only two order parameters - one for structural order η ranging from 0 (disordered phase) to 1 (crystalline state), and the other for crystal orientation field θ . The elegance of the KWC model is offset by the severe restriction it imposes on the grain boundary energy. The energy functional of the KWC model limits the dependence of grain boundary energy on misorientation angle to a Read–Shockley-type (Read and Shockley, 1950) that does not respect the crystal symmetry. In addition, the singular diffusive nature of the KWC model results in stiff equations that are computationally expensive to solve.

Recognizing the elegance of the KWC model, we formulate a generalization of the KWC model that can incorporate arbitrary misorientation-dependent grain boundary energies. In addition, we design a thresholding method that addresses the challenge of solving the singular diffusive equation of the KWC model. The resulting model inherits the memory efficiency of the original KWC model, while having significantly more computational efficiency compared to conventional numerical methods such as finite element and finite difference.

The paper is structured as follows. In Section 2, we discuss the role of crystal symmetry on the anisotropy of grain boundary energies, and review the original KWC model and its limitations. Then, we propose a generalization of the KWC model to incorporate grain boundary energies beyond the Read–Shockley type. In Section 3, we design a thresholding algorithm to implement the generalized KWC model. Numerical experiments to validate and demonstrate the computational efficiency of the thresholding method are discussed in Section 4. Finally, we summarize and conclude with a description of future directions.

²Grain boundary energy as a function of inclination is typically non-convex. For grain boundary models that incorporate inclination dependence to be well-posed, they must include curvature-dependent energy densities resulting in a higher-order model which adds to the computationally intensive nature of the MPF model.

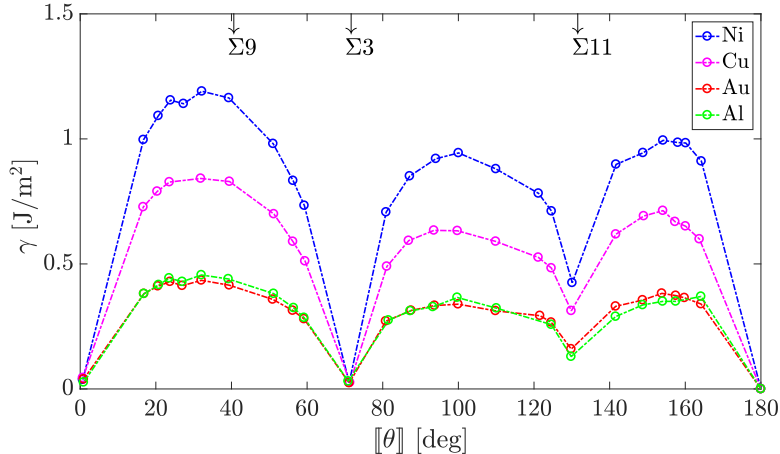


Figure 1: A plot of grain boundary energy density as a function of misorientation angle of a $[110]$ symmetric-tilt grain boundary in fcc copper, computed using molecular dynamics [Holm et al. \(2010\)](#); [Bulatov et al. \(2014\)](#). Misorientations corresponding to low energy Σ boundaries are marked on the upper axis.

2. Grain boundary energy and the Kobayashi–Warren–Carter model

A grain boundary is characterized by five macroscopic degrees of freedom where three degrees represent a rotation associated with the misorientation between the two grains, and the remaining two degrees correspond to the inclination of the grain boundary. More precisely, the grain boundary character space is given by the topological space $\mathcal{T} = SO(3) \times SO(3)/SO(2)$, where $SO(n)$ is the special orthogonal group in n dimensions. Grain boundaries are equipped with a surface energy density, which is defined as a function on \mathcal{T} . An energy density that is constant is referred to as an *isotropic*, and *anisotropic* otherwise. Fig. 1 shows a plot of grain boundary energy density as a function of misorientation angle for a $[110]$ symmetric-tilt grain boundary in face-centered cubic (fcc) copper, calculated using molecular dynamics simulations ([Holm et al., 2010](#); [Bulatov et al., 2014](#)). Since the symmetry of an fcc lattice ensures that the energy of a $[110]$ symmetric-tilt grain boundary is symmetric about the 180° misorientation angle, Fig. 1 shows a plot of energy vs misorientation angles up to 180° . In addition, γ exhibits local minima at certain misorientations, marked as Σ_3 and Σ_{11} in Fig. 1, due to an enhanced lattice matching ([Runnels et al., 2016a,b](#); [Wolf, 1990](#)) between the two adjoining grains. Recent efforts ([Mason and Patala, 2019](#); [Bulatov et al., 2013](#); [Runnels et al., 2016a,b](#); [Olmsted et al., 2009](#); [Kim et al., 2014](#)) by materials scientists in characterizing the grain boundary character space, and parametrizing grain boundary energy using data from atomistic simulations and experiments, bring us closer to developing an atomistically informed mesoscale model for grain boundaries.

The motion of grain boundaries driven by surface tension to decrease the interfacial energy is a defining characteristic of various grain microstructure models such as the Mullins model ([Mullins, 1956](#)), and its diffuse-interface counterparts such as the multiphase field and the KWC models. The resulting grain boundary motion, commonly referred to as *motion by curvature*, in the presence of an anisotropic energy density has been shown to have a considerable effect on grain statistics ([Barmak et al., 2013](#)) leading to changes in the macro-

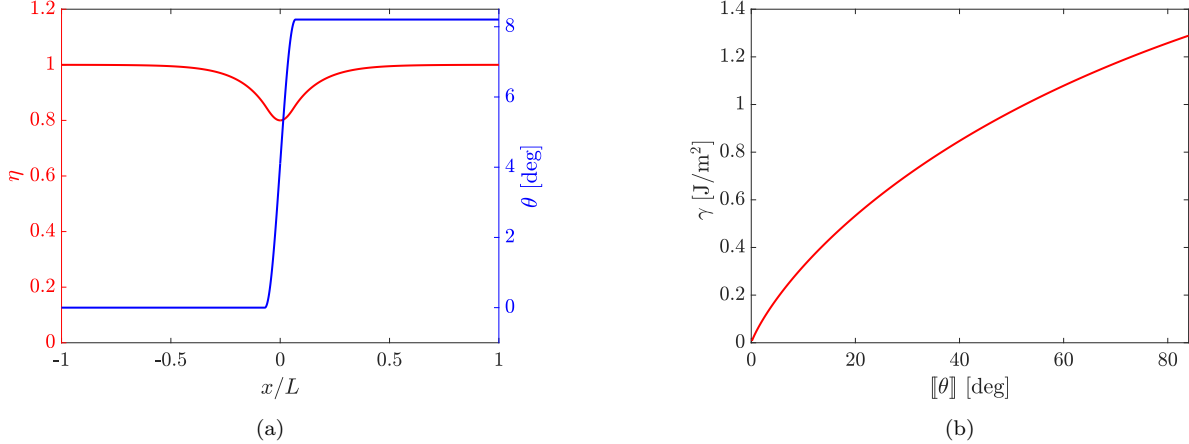


Figure 2: Results on the one-dimensional steady state solution of the original KWC model describing a flat grain boundary. **a)** A steady state analytical solution of the KWC model for a given misorientation. **b)** Variation of the grain boundary energy as a function of misorientation in the KWC model.

scopic properties of materials. In order to explore the structure-property relationship, recent research efforts have focused on developing ultrafast algorithms to simulate grain boundary evolution in large polycrystals in the presence of atomistically derived anisotropic grain boundary energies.

In this paper, we recognize the simplicity of the phase field model of Kobayashi, Warren and Carter, and show that it can be generalized and implemented using a thresholding method resulting in an ultrafast algorithm for grain boundary evolution.

2.1. The KWC model

The Kobayashi–Warren–Carter (KWC) model (Kobayashi et al., 1998, 2000; Warren et al., 2003) is a dual-phase field model to study grain evolution in polycrystalline materials. In this model, an arbitrary polycrystal in two dimensions is described using only two order parameters η and θ . This is one of the main advantages of employing the KWC model as opposed to the multiphase field model, which uses as many order parameter as the number of grains. The order parameter η ranges from 0, which signifies disorder, to 1 that describes crystalline order. On other hand, the order parameter θ describes the orientation of the grains.³

The KWC model is governed by a free energy functional given by

$$\mathcal{W}[\eta, \theta] = \int_{\Omega} \left[\frac{f(\eta)}{\epsilon} + \frac{\epsilon}{2} |\nabla \eta|^2 + g(\eta) |\nabla \theta| + \frac{\epsilon}{2} |\nabla \theta|^2 \right] dV, \quad (2.1)$$

where

$$f = \frac{(1 - \eta)^2}{2} \quad (2.2)$$

³In three dimensions, the order parameter θ is replaced by a rotation tensor.

is a single-well potential with minimum at $\eta = 1$, and

$$g = -\ln(1 - \eta) \quad (2.3)$$

is an increasing function.⁴ The functional in (2.1) is defined for all functions η and θ in the Hilbert space $H^1(\Omega)$.⁵ The constant $\epsilon > 0$ is a dimensionless scaling parameter that determines the thickness of the grain boundary region (Lobkovsky and Warren, 2001). The evolution equations for the order parameters, assuming a gradient descent (with respect to the L^2 -norm) of \mathcal{W} , are obtained as

$$\epsilon b_\eta \dot{\eta} = \epsilon \Delta \eta - \frac{f'(\eta)}{\epsilon} - g'(\eta) |\nabla \theta|, \quad (2.4a)$$

$$\epsilon b_\theta \dot{\theta} = \nabla \cdot \left[\epsilon \nabla \theta + g(\eta) \frac{\nabla \theta}{|\nabla \theta|} \right], \quad (2.4b)$$

where b_η and b_θ are the inverse mobilities corresponding to respective order parameters.⁶

A one-dimensional steady state solution of (2.4) under Dirichlet boundary conditions is plotted in Fig. 2a. The value of $\eta < 1$ in a neighborhood of the grain boundary suggests a loss of crystalline order, and the orientation θ is constant in the interior of the grains, and has a non-zero gradient in a finite thickness around the grain boundary. In the limit $\epsilon \rightarrow 0$, Lobkovsky and Warren (2001) have shown that the evolution equations in (2.4) result in the shrinking of the grain boundary thickness converging to the Mullins model.

Below, we briefly summarize the role of each term appearing in the KWC functional. We refer the reader to Warren et al. (2003) for a more detailed description, and Admal et al. (2019) for a generalization of the KWC model to three dimensions. The function f drives $\eta(\mathbf{x})$ towards 1, while the coupled term $g(\eta) |\nabla \theta|$ tends to decrease η in a neighborhood of the grain boundary. In addition, the coupled term tends to localize the jump in θ , while $|\nabla \theta|^2$ has a tendency to diffuse it, resulting in a regularized step function for θ . It is interesting to note that in the absence of the $|\nabla \theta|^2$ term, the steady state solution for θ is a pure step function, resulting in a model with a blend of sharp- and diffuse-interface characteristics, i.e. while θ is sharp, η is diffused. Moreover, grain boundaries cease to evolve in the absence of $|\nabla \theta|^2$ term (Lobkovsky and Warren, 2001). In other words, $|\nabla \theta|^2$ in the KWC model has a dual role of not only regularizing θ but also rendering non-zero mobility to the grain boundaries.

The grain boundary energy γ , as a function of misorientation angle, predicted by the KWC model is of the Read-Shockley-type, as shown in Fig. 2b. This is in contrast to the experimentally observed grain boundary energies shown in Fig. 1. Despite the elegance of the KWC model in describing polycrystals with only two order parameters, its restriction to

⁴The choice of the logarithmic function for g is supported by the work of Alicandro et al. (1999), which shows that the KWC functional converges (in the sense of Γ -convergence) to a surface energy function when $g(1) = \infty$ (See Theorem 4.1 in Alicandro et al. (1999)).

⁵ $H^1(\Omega)$ denotes the set of all functions on Ω whose first derivatives are square integrable.

⁶The KWC model was originally developed to simultaneously model grain rotation *and* grain boundary motion. The model can be specialized to demonstrate *only* grain boundary motion by enforcing zero mobility for θ in the grain interior. This can be achieved by a constant b^ϕ , and a ϕ -dependent b^θ (Dorr et al., 2010).

Read–Shockley type grain boundary energies is a major limitation compared to the flexibility of incorporating arbitrary grain boundary energies into the multiphase field model. The above-stated limitation is one of the main motivation for us to seek a new formulation of the KWC model to incorporate arbitrary misorientation-dependent grain boundary energies that respect the bicrystallography of grain boundaries.

2.2. A crystal symmetry-invariant KWC model

In this section, we formulate a new KWC model that can incorporate arbitrary misorientation-dependent grain boundary energies.

We begin with the KWC functional without the $|\nabla\theta|^2$ term. From Section 2.1, recall that in the absence of the $|\nabla\theta|^2$ term, the steady state solution for θ is a step function with the discontinuity occurring at the grain boundary. In one-dimension, since a discontinuous θ is not in $H^1(\Omega)$, the minimizer of \mathcal{W} , with $|\nabla\theta|^2$ absent, is not attained. This observation motivates us to redefine the domain of the modified KWC functional such that θ belongs to the space of piecewise constant functions, as opposed to $H^1(\Omega)$, and this enables us to simplify the functional as

$$\mathcal{W}[\eta, \theta] = \int_{\Omega} \left[\frac{(1-\eta)^2}{2\epsilon} + \frac{\epsilon}{2} |\nabla\eta|^2 \right] dV - \int_{\mathcal{S}} \ln(1-\bar{\eta}) [[\theta]] dS, \quad (2.5)$$

where $\bar{\eta} : \mathcal{S} \rightarrow \mathbb{R}$ is the restriction of η to the jump set \mathcal{S} of θ , which represents the union of all grain boundaries. The steady state solution, given in (A.8), corresponding to a one-dimensional bicrystal governed by (2.5), and the resulting grain boundary energy as a function of the misorientation,

$$\gamma([\theta]) = \frac{[[\theta]]}{2} \left(1 - 2 \ln \left[\frac{[[\theta]]}{2} \right] \right) \quad (2.6)$$

are derived in Appendix A. From (2.6), it is clear that the grain boundary energy is of a Read–Shockley-type, which does not respect the crystal symmetry.

The above observation leads us to the following generalization of the KWC functional

$$\mathcal{W}^G[\eta, \theta] = \int_{\Omega} \left[\frac{(1-\eta)^2}{2\epsilon} + \frac{\epsilon}{2} |\nabla\eta|^2 \right] dV + \int_{\mathcal{S}} g(\bar{\eta}) \mathcal{J}([\theta]) dS, \quad (2.7)$$

which is defined for all $\eta \in H^1(\Omega)$, and piecewise constant functions θ ; and \mathcal{J} is an even function of the jump in orientation. Under this new formulation, the grain boundary energy function modifies as

$$\begin{aligned} \gamma^G([\theta]) &= (1-\bar{\eta})^2 - \ln(1-\bar{\eta}) \mathcal{J}([\theta]) \\ &= \frac{\mathcal{J}([\theta])}{2} \left(1 - 2 \ln \left[\frac{\mathcal{J}([\theta])}{2} \right] \right), \end{aligned} \quad (2.8)$$

where $\bar{\eta}$ is the value of the steady-state solution on the grain boundary, given implicitly in

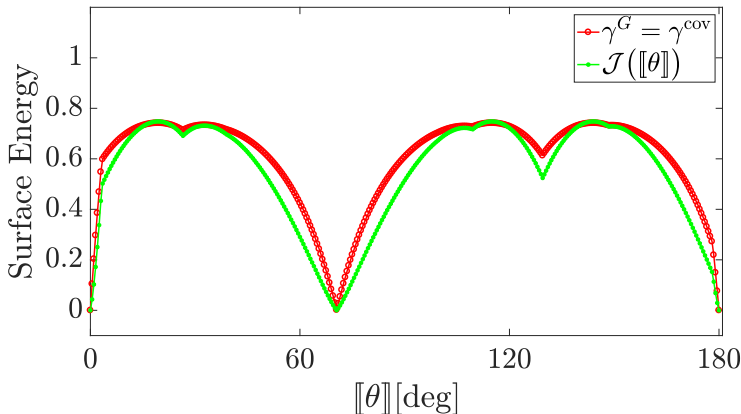


Figure 3: A plot (in green) of the core energy $\mathcal{J}(\llbracket\theta\rrbracket)$ calculated to match γ^G (2.8) to γ^{cov} (B.9) (in red) for $[110]$ symmetric-tilt grain boundaries in fcc copper. γ^G is identical to γ^{cov} by construction.

terms of $\mathcal{J}(\llbracket\theta\rrbracket)$ as⁷

$$2(1 - \bar{\eta})^2 = \mathcal{J}(\llbracket\theta\rrbracket). \quad (2.9)$$

Inspired from the terminology in dislocations, we refer to $\mathcal{J}(\llbracket\theta\rrbracket)$ as the *core energy*.

From (2.8), it is clear that by appropriately constructing the core energy \mathcal{J} , we can arrive at a γ^G that faithfully represents the grain boundary energy and symmetry of the bicrystal. In other words, the crystal symmetry of the new KWC model is inherited from the core energy. For illustration, we consider the energy γ^{cov} of a $[110]$ symmetric tilt grain boundary in face-centered cubic (fcc) copper, shown as red data points in Fig. 3. γ^{cov} is computed using the *covariance model* developed by Runnels et al. (2016a,b), wherein it is defined as the covariance of the two lattices adjoining the grain boundary. For completeness, in Appendix B, we describe the covariance model of grain boundary energy, the procedure to compute it, and list the parameters used to arrive at the data plotted in Fig. 3. We solve for \mathcal{J} in (2.8) using the Newton’s method such that the resulting $\gamma^G = \gamma^{\text{cov}}$ at each data point. In other words, the grain boundary energy of the resulting KWC model is identical to γ^{cov} by construction. Fig. 3 shows a plot of the solution \mathcal{J} in green, and highlights the common positions of the local minimizers of \mathcal{J} and γ^{cov} . Typically, the number of Newton iterations for convergence error (absolute value of the difference between γ^G and γ^{cov}) of $10^{-6}[\text{J}/\text{m}^2]$ is less than 20. While the modification of the KWC functional from (2.5) to (2.7) allows us to model arbitrary misorientation-dependent grain boundary energies, the absence of $|\nabla\theta|^2$ term in (2.7) renders the grain boundaries immobile as mentioned in Section 2.1.⁸ In what follows, we address this shortcoming by devising a thresholding method to move grain boundaries by evolving the piecewise-constant θ .

⁷The analog of (2.9) in the original KWC model is (A.7), whose derivation is shown in Appendix A.

⁸The evolution of θ by the gradient descent of \mathcal{W}^G results in pure rotation while the position of the grain boundaries remains fixed.

3. Grain boundary motion in the new KWC model

In this section, we present our approach in which we alternate between evolving η and θ to evolve a polycrystal governed by \mathcal{W}^G . The order parameter η is solved in the following minimization problem for a given θ

$$\eta^* = \arg \min_{\substack{\eta \in H^1(\Omega) \\ \partial\eta/\partial n|_{\partial\Omega}=0}} \mathcal{W}^G[\eta, \theta]. \quad (3.1)$$

Next, the orientation field θ is evolved using a thresholding rule described in the next section.

In order to solve for η in (3.1), we note that since $g(\eta) \rightarrow \infty$ as $\eta \rightarrow 1$, the functional \mathcal{W}^G is non-smooth in η , which makes the Newton's method not viable. Therefore, we use a primal-dual method recently developed by [Jacobs et al. \(2019\)](#), which has a $\mathcal{O}(\frac{1}{\epsilon} N \log N)$ complexity, where ϵ is the error in the numerical solution to (3.1), and N is the grid size. See [Appendix C](#) for a more detailed description of the primal dual method.

Next, we develop a thresholding rule to evolve θ for a fixed η^* obtained in (3.1). The alternate use of the primal dual method and the thresholding rule at every time step constitutes our approach to evolving the grain boundaries.

3.1. The thresholding rule

A thresholding method is a sequence of simple rules, executed every time step to reinitialize the order parameter, such that its evolution describes the motion of a grain boundary.

The original idea of using a thresholding method to evolve grain boundaries goes back to the work ([Merriman et al., 1992](#)) of Merriman, Bence and Osher (MBO) wherein, similar to the multiphase field model, grains in a polycrystal are described using as many order parameters, with the caveat that the order parameters are piecewise-constant implying a sharp interface. An order parameter in the MBO method is evolved based on a two-step thresholding scheme — a convolution of the order parameter with a Gaussian kernel followed by a trivial thresholding — resulting in motion by curvature.

The MBO method has recently been generalized by [Esedoglu and Otto \(2015\)](#) to a variational model, referred to as the *Gaussian kernel method*. In the MBO and the Gaussian kernel methods, there are as many characteristic functions as the number of distinct grains. While the end goal of the KWC model is also to describe motion by curvature, it is markedly different from the Gaussian kernel method as it uses only two order parameters to represent a polycrystal. Therefore, it does not require additional techniques to address the memory intensive nature of a naive implementation of the MBO/Gaussian kernel methods. More importantly, the KWC model lends itself to further generalizations which include the modeling of grain rotation. Therefore, the goal here is to seek a thresholding algorithm to implement the KWC model.

In this section, we design a thresholding rule for θ that results in motion by curvature. We first recall that θ is a piecewise-constant field with a finite range of orientations. This implies, that a thresholding rule for θ reassigns $\theta(\mathbf{x})$, for each point $\mathbf{x} \in \Omega$, to one of the possible orientations. Our thresholding rule originates from the observation that *the asymmetry of η in the neighborhood of a grain boundary characterizes its curvature*. Below, we explicitly identify this asymmetry before describing our thresholding rule.

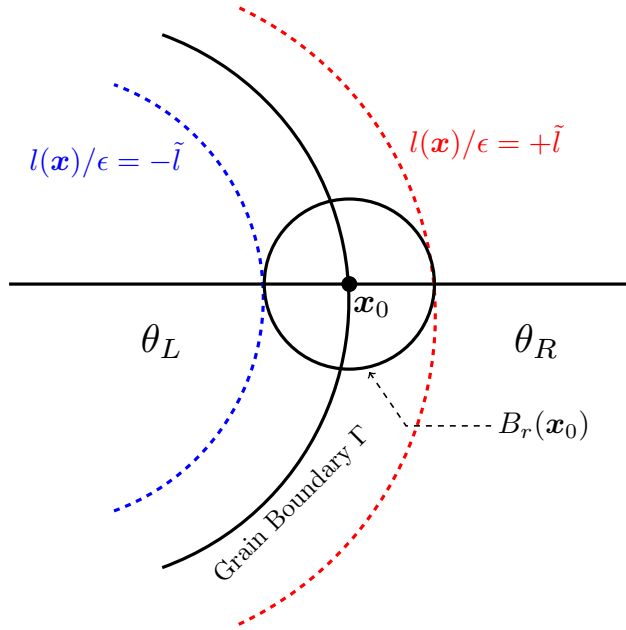


Figure 4: Level sets of the distance function $l(\mathbf{x})$ in a neighborhood of \mathbf{x}_0 . The grain boundary Γ is depicted as a solid curve, and the dashed curves correspond to the level sets $l(x)/\epsilon = \pm\tilde{l}$.

First, we note that the steady-state solution for η , derived in (A.8) for a flat interface (zero curvature), is symmetric about the grain boundary. Next, we derive an approximate form for η in the presence of a non-zero curvature, and show the dependence of asymmetry on the curvature. Let Γ denote a grain boundary with a non-zero curvature that separates two grains with orientations θ_L and θ_R . We postulate that for a Γ with a small curvature such that $\epsilon\kappa \ll 1$, and for a $\mathbf{x}_0 \in \Gamma$ away from a triple junction, the solution η^* to (2.4a) is approximated in a small neighborhood of \mathbf{x}_0 as

$$\eta^*(\mathbf{x}) \approx u\left(\frac{l(\mathbf{x})}{\epsilon}\right), \quad (3.2)$$

where $l(\mathbf{x})$ is the signed distance function from Γ to \mathbf{x} , as shown in Fig. 4. In other words, we assume that η only depends on the radial coordinate. Away from the grain boundary, the solution to the minimization problem in (3.1) satisfies the equation

$$\epsilon\Delta\eta^* - \frac{(\eta^* - 1)}{\epsilon} = 0. \quad (3.3a)$$

The above equation can be simplified by using a local coordinate system $\mathbf{x} = (\tilde{l}, s)$, where $\tilde{l} = l(\mathbf{x})/\epsilon$ is the scaled radial coordinate, and s is the distance measured along Γ between \mathbf{x}_0 and the perpendicular projection of \mathbf{x} on Γ . In this coordinate system, we note that $\Delta\eta(\mathbf{x}) = u''/\epsilon^2 + \kappa u'/\epsilon$, where $\kappa(\tilde{l})$ is the curvature of the coordinate line $\{\mathbf{x} \in B_r(\mathbf{x}_0) : l(\mathbf{x}) = \tilde{l}\epsilon\}$. Therefore, (3.3) simplifies as

$$u''(\tilde{l}) + \epsilon\kappa u'(\tilde{l}) - u(\tilde{l}) + 1 = 0. \quad (3.4)$$

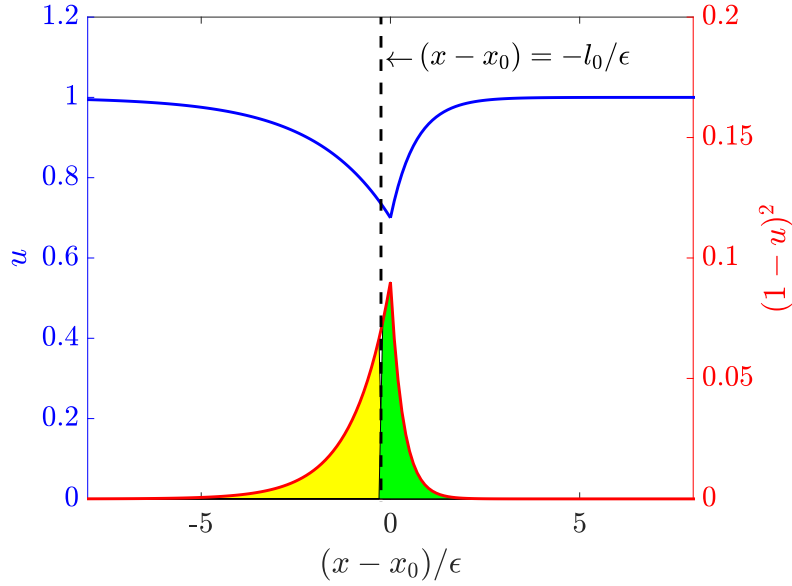


Figure 5: A plot of η^* in a small neighborhood of x_0 (see Fig. 4) is shown in blue, while $(1 - \eta^*)^2$ is shown in red. The asymmetry of u around x_0 due to curvature κ is characterized by the position x at which the two areas shown in yellow and green regions are equal. The position x is given in terms of l_0 ($(x - x_0) = l_0/\epsilon$), which is the solution of (3.7).

Assuming $\kappa(\tilde{l}) = \kappa(0)$, we obtain the following closed form solution to (3.4):

$$u(\tilde{l}) = 1 + C_1 \exp \left[-\tilde{l} \left(\frac{\epsilon\kappa + \sqrt{4 + \epsilon^2\kappa^2}}{2} \right) \right] + C_2 \exp \left[-\tilde{l} \left(\frac{\epsilon\kappa - \sqrt{4 + \epsilon^2\kappa^2}}{2} \right) \right], \quad (3.5)$$

where the constants C_1 and C_2 are determined using the boundary conditions $u(\pm\infty) = 1$.⁹ Subsequently, the solution can be further approximated¹⁰ under the assumption that both ϵ and $\epsilon\kappa$ are small, resulting in

$$u(\tilde{l}) = \begin{cases} 1 + (u(0) - 1)e^{-(1+0.5\epsilon\kappa)\tilde{l}} & \text{if } \tilde{l} > 0, \\ 1 + (u(0) - 1)e^{(1-0.5\epsilon\kappa)\tilde{l}} & \text{otherwise.} \end{cases} \quad (3.6)$$

The asymmetry of u is apparent from (3.6) by noting that in the presence of a positive curvature, the rate at which $u \rightarrow 1$ as $\tilde{l} \rightarrow +\infty$ is greater than when $\tilde{l} \rightarrow -\infty$.

The asymmetry of u forms the foundation of our thresholding scheme, which is designed to reassign the values of θ in the neighborhood of the grain boundaries resulting in a motion

⁹The boundary conditions are interpreted in the limit $\epsilon \rightarrow 0$, which results in the boundary conditions $l/\epsilon = \pm\infty$ for the scaled radial coordinate.

¹⁰Here, we use the approximation $\sqrt{4 + \epsilon^2\kappa^2} \approx 2 + \mathcal{O}(\epsilon^2\kappa^2)$.

by curvature. To design a thresholding rule, we identify a unique $l = l_0$, such that

$$\int_{-\infty}^{l_0} (1 - u(l/\epsilon))^2 dl = \int_{l_0}^{+\infty} (1 - u(l/\epsilon))^2 dl. \quad (3.7)$$

The two integrals in (3.7) are depicted as equal areas under the yellow and green regions in Fig. 5, which clearly shows that in the presence of a non-zero curvature, the asymmetry of u results in $l_0 \neq 0$. A straightforward but tedious calculation (see Appendix D for details) shows that

$$l_0 = -\frac{\epsilon^2}{4}\kappa + \mathcal{O}(\epsilon^3). \quad (3.8)$$

By reinitializing the orientations of all \mathbf{x} with $l(\mathbf{x}) < l_0$ to θ_L , and to θ_R when $l(\mathbf{x}) > l_0$, we have a thresholding rule that moves the grain boundary by $\epsilon^2\kappa$ in one time step $dt = \mathbf{t}\epsilon^2/4$, where $\mathbf{t} = 1$ is a unit conversion factor. Alternating between the η -update using the primal-dual method, and the θ -update using the thresholding rule, results in a grain boundary motion by curvature with mobility equal to the inverse of the grain boundary energy.¹¹ Although this is a severe restriction on the mobility, we postulate that this can be overcome by modifying the thresholding rule (3.7), and this will be addressed in a future work. The efficiency of the thresholding rule described above rests on the computation of l_0 in (3.7). In the next section, we use the *fast marching method* to not only compute l_0 in an $\mathcal{O}(N \log N)$ algorithm, but also generalize the above strategy to an arbitrary polycrystal.

3.2. Thresholding dynamics via the fast marching method

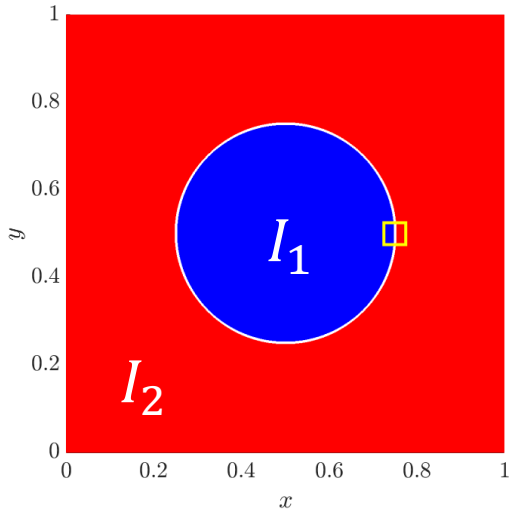
The fast marching method (FMM), developed by Tsitsiklis (1995), is an algorithm to evolve a surface with a spatially varying normal velocity. A general description of FMM with a stand-alone example is given in Appendix E. Here, we focus on using the fast marching method to implement the thresholding algorithm described in Section 3.1 by solving for l_0 in (3.7).

We begin with a description of our implementation of the thresholding scheme for a bicrystal consisting of a circular grain, followed by its generalization to a polycrystal. We first recall that the boundary conditions $u(\pm\infty) = 1$ used to arrive at (3.6)–(3.7) apply only in the limit $\epsilon \rightarrow 0$ as noted in footnote 9. In practice, we choose a finite limit $l_b > 0$, and modify (3.7) as

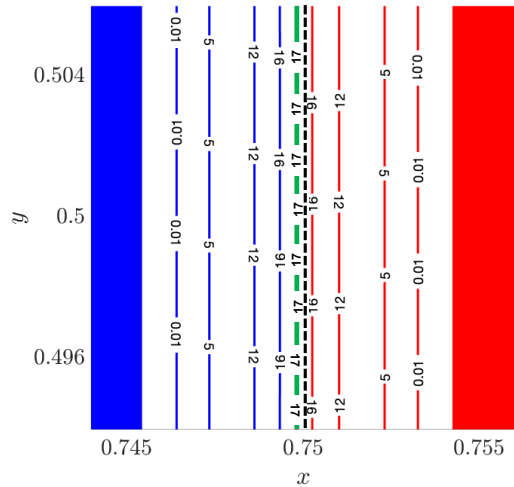
$$\text{Find } l_0 \text{ such that } \int_{-l_b}^{l_0} (1 - u(l/\epsilon))^2 dl = \int_{l_0}^{l_b} (1 - u(l/\epsilon))^2 dl. \quad (3.9)$$

In Appendix D, we show that the error in l_0 due to the introduction of l_b exponentially decreases as $\epsilon \rightarrow 0$. In order to use FMM to compute l_0 , we interpret the integrand $(1 - u(l/\epsilon))^2$ in (3.9) as an inverse of the normal velocity of a surface $\mathcal{S}_l := \{\mathbf{x} : l(\mathbf{x}) = l\}$ traveling towards the grain boundary. Under this interpretation, the integrals in (3.9) are a measure of the time it takes for two initial surfaces \mathcal{S}_{-l_b} and \mathcal{S}_{l_b} on either side of the grain boundary,

¹¹In this case, the *reduced mobility* (Salvador and Esedoğlu, 2019; Martine La Boissonière et al., 2019), which is defined as the product of grain boundary energy and mobility, is equal to 1 for all grain boundaries.



(a) Two interior regions of a bicrystal.



(b) The evolution of ∂I_1 and ∂I_2 solved using the fast marching method.

Figure 6: Shrinking of a circular grain simulated using the thresholding method. **a**) Two interior regions (red and blue) I_1 and I_2 are grown towards the grain boundary with a speed $1/(1 - \eta^*)^2$ using the fast marching method. **b**) A closeup of a rectangular region around the grain boundary, depicted in **a**), shows the contour lines of the fast marching method, which describe the time it takes for ∂I_1 or ∂I_2 to arrive at a grid point. Therefore, the original grain boundary, shown as a dashed black line in **b**), moves to a new position (solid green line) where the two grain interiors meet.

to meet at $l = l_0$. We use the fast marching method to evolve the surfaces \mathcal{S}_{-l_b} and \mathcal{S}_{l_b} , and implement the thresholding rule described in Section 3.1 by reassigning the orientation of any point \mathbf{x} in the region $\{\mathbf{x} \in \Omega : |l(\mathbf{x})| < l_b\}$ to θ_L if it first encounters the evolving surface \mathcal{S}_{-l_b} , and to θ_R otherwise.

In practice, however, we do not have access to the signed distance function $l(\mathbf{x})$ to identify the surfaces \mathcal{S}_{-l_b} and \mathcal{S}_{l_b} . Instead, we first identify the grain interiors I_p defined as

$$I_p = \{\mathbf{x} \in \Omega : \theta(\mathbf{x}) = \theta_p, \eta(\mathbf{x}) > 1 - \xi\}, \quad (3.10)$$

where $\xi > 0$ is some fixed small value. Fig. 6a shows the grain interiors I_1 and I_2 in a bicrystal, and Fig. 6b is a closeup of a rectangular region, marked in yellow, around the grain boundary. The original grain boundary is marked as a black dashed line in Fig. 6b. By construction, the two surfaces ∂I_1 and ∂I_2 are equidistant, up to $\mathcal{O}(\epsilon)$, from the grain boundary, and serve as substitutes for \mathcal{S}_{-l_b} and \mathcal{S}_{l_b} . The grain interiors are grown in the outward direction with a velocity $(1 - u(l/\epsilon))^{-2}$ using the fast marching method, and the surface where they meet is the new grain boundary, shown as a green dashed line in Fig. 6b.

We will now generalize the above implementation to an arbitrary polycrystal consisting of \mathcal{N} grains, described using a piecewise constant θ with values in $\{\theta_1, \dots, \theta_{\mathcal{N}}\}$. Using (3.10), we identify the \mathcal{N} grain interiors, and define I as their union. Next, we grow the grain interiors in their outward unit normal directions until every point (in the almost everywhere sense) in the domain is in precisely one grain. We implement this by first collecting all the boundaries of the interior regions in $\partial I = \partial I_1 \cup \dots \cup \partial I_n$, and *simultaneously* evolving

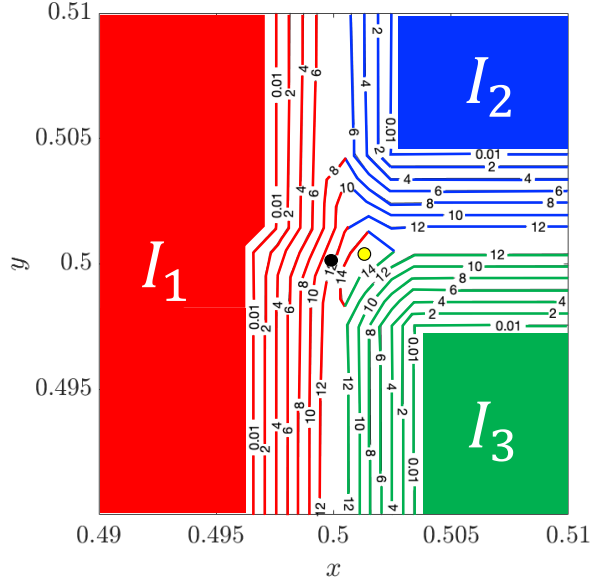


Figure 7: Movement of a triple junction according to the thresholding algorithm. The triple junction initially at $(x, y) = (0.5, 0.5)$ (black filled circle) moves to a new position (yellow filled circle) where the three grain interiors, evolved using the fast marching method, meet at the same time.

them in the outward normal direction with a speed of $1/(1 - \eta^*(x))^2$ using the fast marching method.¹² As the grain interiors grow, a point $\mathbf{x} \in \Omega - I$ is reinitialized to an orientation θ_q if it encounters $\partial I_q \subset \partial I$. At the end of the fast marching method, all points in $\Omega - I$ have been reinitialized resulting in an updated polycrystal at the end of a time step. Fig. 7 shows the implementation of the thresholding rule in a tricrystal. Dirichlet boundary conditions on θ are imposed by including all $\mathbf{x} \in \partial\Omega$ in the grain interiors. On the other hand, periodic boundary conditions are achieved by periodically reinitializing θ for $\mathbf{x} \in \partial\Omega$ during the fast marching step.

The primal-dual and the fast marching methods are implemented on a regular grid of resolution, say δx . From (3.8), we know that the resolution of the grid should be large enough to resolve a grain boundary movement of $\epsilon^2 \kappa$ in each time step, i.e.

$$\delta x \ll \epsilon^2 \kappa, \quad (3.11)$$

which is a common requirement of other thresholding methods (Esedoğlu and Otto, 2015; Merriman et al., 1992). If this condition is not satisfied, grain boundaries would stagnate. Since grain boundary evolution results in an overall decrease in curvature, (3.11) may cease to hold as the simulation progresses. Therefore, we adaptively increase ϵ when a grain boundary stagnates, and as a consequence, we obtain a time adaptive algorithm since $dt \propto \epsilon^2$. On the other hand, an extremely small ϵ will increase the computational cost of the thresholding

¹²Note that the fast marching method is used to evolve *all* grain interiors in unison as opposed to evolving them individually.

Algorithm 1: Thresholding algorithm for the new KWC model

Input : A polycrystal with \mathcal{N} grains with orientations $\theta_1, \dots, \theta_{\mathcal{N}}$, grain boundary core energies $\mathcal{J}(\llbracket\theta\rrbracket)$; parameters: ϵ , ξ , total time T , and tolerance \mathbf{e} .

Output: Time evolution of the polycrystal

Construct the core energy function $\mathcal{J}(\llbracket\theta\rrbracket)$ from grain boundary energy data

Initialize $t = 0$, and the orientation field $\theta(\mathbf{x}, 0)$

while $t < T$ **do**

 Compute the discrete jump fields $\llbracket\theta\rrbracket(\mathbf{x}, t)$ and $\bar{\mathcal{J}} := \mathcal{J}(\llbracket\theta\rrbracket(\mathbf{x}, t))$ on Ω

 Regularize the jump field: $\mathcal{J}^* = G * \bar{\mathcal{J}}$, where $G(\mathbf{x}) = (1/2\pi\epsilon^2)e^{-\frac{|\mathbf{x}|^2}{2\epsilon^4}}$

 // Solve for $\eta(\mathbf{x}, t)$ using the primal-dual algorithm

 Initialize η and the dual field ψ : $\eta_0(\mathbf{x}) = 0$, $\psi_0(\mathbf{x}) = 0$, and $n = 0$

do

$n = n + 1$

 Calculate η_n using ψ_{n-1} (C.6)

 Calculate ψ_n using η_n (C.7)

while $\|\eta_{n+1} - \eta_n\|_{\infty} \leq \mathbf{e}$;

$\eta(\mathbf{x}, t) = \eta_{n+1}$

 // Threshold/update the orientation field

 Identify interiors of grains: $I_p = \{\mathbf{x} \in \Omega : \theta(\mathbf{x}, t) = \theta_p, \bar{\mathcal{J}}(\mathbf{x}) < \xi\}$, and set

$I = \cup_{p=1}^n I_p$

 Evolve I with speed $1/(1 - \eta(\mathbf{x}, t))^2$ using the fast marching method and update/threshold the orientations at each point $\mathbf{x} \in \Omega - I$

$t = t + 0.25\epsilon^2$ (3.8)

end

method.

Finally, we explore the effect of ξ , introduced in (3.10), on the extent to which (3.8) is satisfied. Recall that ξ was introduced in (3.10) to identify grain interiors. In the case of a circular grain (see Fig. 6a), (3.8) implies the rate of change of radius is given by

$$\dot{R}(t) = -\frac{\epsilon^2}{4R(t)}. \quad (3.12)$$

To test if the above equation is satisfied, we executed the thresholding algorithm using the η -solution from the primal dual algorithm with $\epsilon = 0.01$, and measured $\dot{R}(t)$. Relative % errors in shrinking-rate \dot{R} at different values of ξ are summarized in Tab. 1. It is confirmed that for a sufficiently small grid, $\xi = 0.05$ is small enough to achieve an error less than 1%.

Algorithm 1 summarizes our approach. The core energy data \mathcal{J} (e.g., Fig. 3) is computed separately using the procedure described in Section 2.2, and used as an input to our method. The algorithm alternates between the primal-dual and the fast marching methods resulting

	Grid Size	
ξ	1024×1024	2048×2048
0.15	9.77 %	2.32 %
0.10	7.74 %	1.24 %
0.05	3.39 %	0.71 %
0.02	2.58 %	0.07 %

Table 1: The effect of parameter ξ on deviations from the expected motion by curvature. We note that for a 2048×2048 grid, $\xi = 0.05$ is small enough to achieve an error less than 1%.

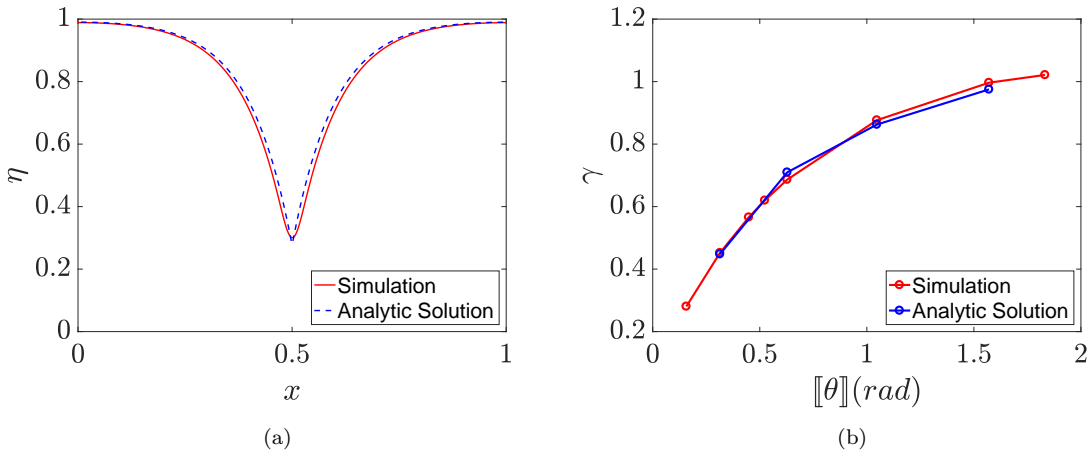


Figure 8: A comparison of the numerical solution resulting from the thresholding algorithm, implemented with $\epsilon = 0.1$ on a 512×512 grid, with the analytical solution. Plots of a) the steady-state solution η , and b) grain boundary energy as a function of misorientation.

in motion by curvature. A C++ template library that implements Algorithm 1 is available at <https://github.com/admal-research-group/GBthresholding>.

Finally, we remark on the computation of $\mathcal{J}(\mathbf{x})$ on a grid. Since $[[\theta]]$, calculated at a grid point ij in either x - or y -directions using centered-difference, is shared between two grid points, a factor of $1/2$ appears in the following expression used to compute the total jump:

$$[[\theta]]_{ij} = \frac{1}{2} \sqrt{(\theta_{i+1,j} - \theta_{i-1,j})^2 + (\theta_{i,j-1} - \theta_{i,j+1})^2}. \quad (3.13)$$

4. Numerical results

In this section, we present examples that explore various features of grain boundary evolution predicted by our model.

We begin with a simulation of a one-dimensional bicrystal $\Omega = [0, 1]$ with a grain boundary at $x = 0.5$, and $\mathcal{J}([[\theta]]) = [[\theta]]$. The purpose of this simulation is to ensure that the results of the primal dual algorithm are consistent with the analytical model described in Appendix A. A Neumann boundary condition $d\eta/dx = 0$ is enforced at the two ends. In the absence of a curvature, we expect the grain boundary to remain at $x = 0.5$, and η reach its steady state. The tolerance \mathbf{e} of the primal dual algorithm (C.8) is set to 10^{-6} . Fig. 8a confirms the agreement between η obtained from the primal dual algorithm and the analytical form

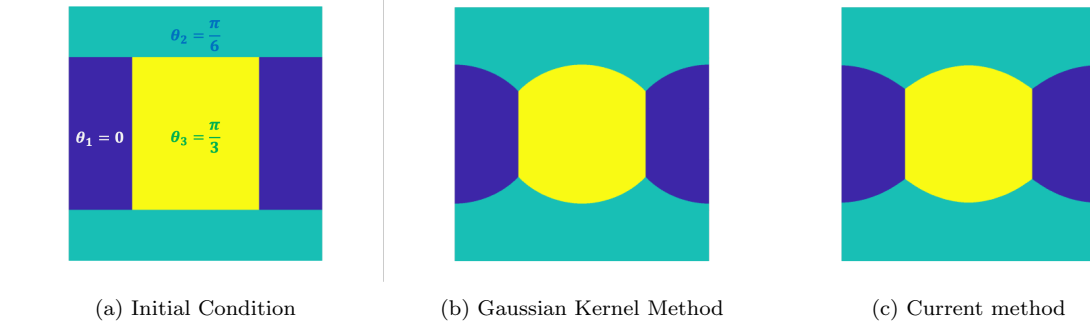


Figure 9: A comparison of the evolutions of a tricrystal under periodic boundary conditions obtained using the Gaussian kernel method and the generalized KWC model with $\epsilon = 0.01$, implemented using our method. The dihedral angles predicted by the Gaussian kernel method and our method are $(93^\circ, 133.5^\circ, 133.5^\circ)$ and $(106^\circ, 127^\circ, 127^\circ)$ respectively, while the theoretical values are $(90.89^\circ, 134.56^\circ, 134.56^\circ)$. In Fig. 10, we demonstrate that the error in the dihedral angles predicted by the generalized KWC model decreases as $\epsilon \rightarrow 0$.

given in (A.8). Furthermore, Fig. 8b shows that the grain boundary energies predicted by the primal-dual algorithm for various misorientation angles are in agreement with the analytical result in (A.10).

4.1. Equilibrium of a triple junction

A triple junction is a line where three grains meet, and it is represented as a point in two dimensions. The equilibrium of a triple junction is guaranteed if it satisfies the Herring relation (Herring, 1951) given by

$$\frac{\gamma^{12}}{\sin \Theta_3} = \frac{\gamma^{23}}{\sin \Theta_1} = \frac{\gamma^{31}}{\sin \Theta_2}, \quad (4.1)$$

where Θ_i is the dihedral angle of grain i , and γ^{ij} is the energy density of the grain boundary shared by grains i and j . While the Herring relation is derived in the sharp-interface framework, it is also seen to hold for a triple junction governed by the original KWC model through (2.4). This is not surprising since the KWC model converges to the Mullins model in the sharp-interface limit *and* the evolution in (2.4) has a variational structure in the form of a gradient descent of the functional in (2.1). On the other hand, it is not clear if our approach to evolve the generalized KWC model arises from a variational formulation. Therefore, it is necessary to examine the Herring relation using our thresholding algorithm. We will now demonstrate that the Herring relation indeed holds provided the parameter ϵ is chosen appropriately.

We study the evolution of a triple junction in a tricrystal with orientations $\theta_1 = 0$, $\theta_2 = \pi/6$, and $\theta_3 = \pi/3$ in $\Omega = [0, 1] \times [0, 1]$. Using the Read–Shockley core energy $\mathcal{J} = \llbracket \theta \rrbracket$, we note from Fig. 8b that the energy density of the three grain boundaries are $\gamma^{12} = 0.62$, $\gamma^{23} = 0.62$, and $\gamma^{13} = 0.87$. From the Herring relation in (4.1), it follows that the steady state dihedral angles are $\Theta_1 = 134.56^\circ$, $\Theta_2 = 90.89^\circ$, and $\Theta_3 = 134.56^\circ$. In order to examine the Herring relation, we consider a tricrystal under periodic boundary conditions, with an

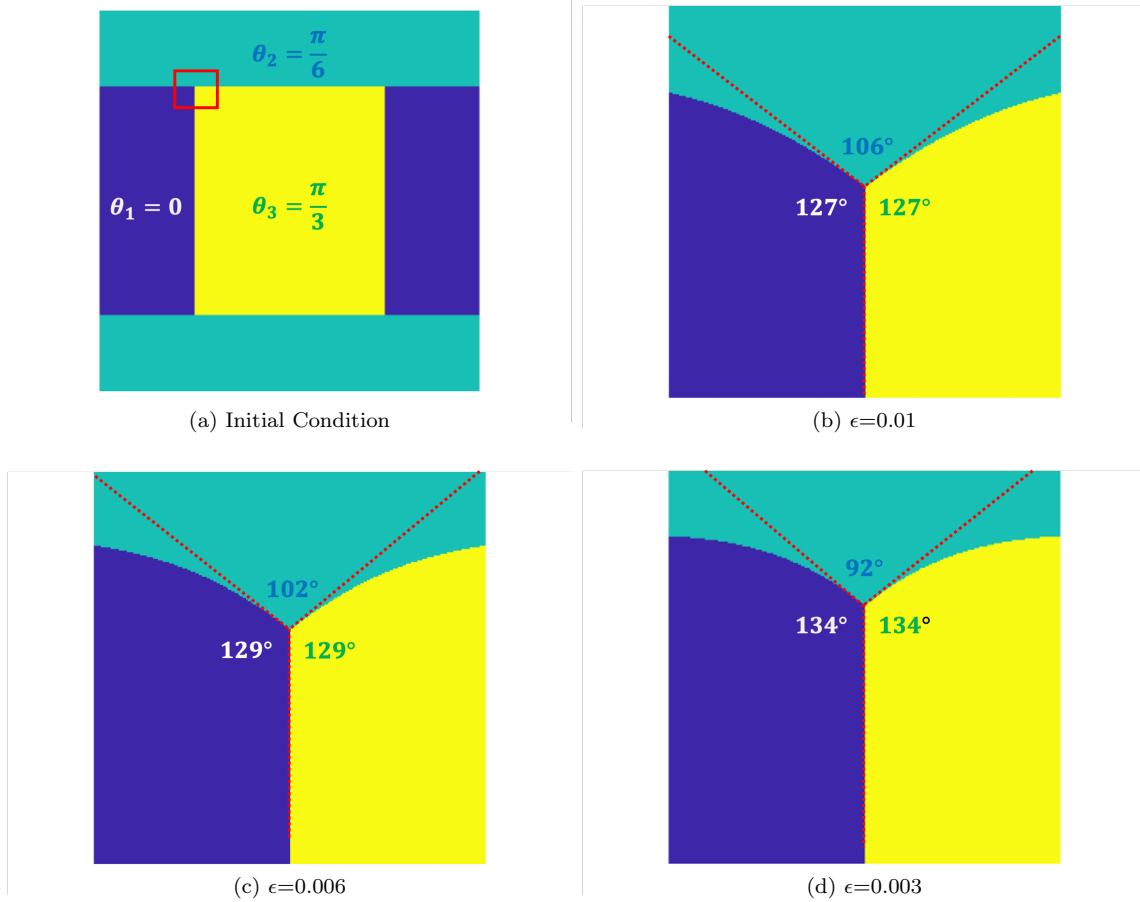


Figure 10: **a)** The orientation distribution in an initial tricrystal under periodic boundary conditions with a triple junction at $(x, y) = (0.25, 0.75)$, and dihedral angles $(\Theta_1, \Theta_2, \Theta_3) = (90^\circ, 180^\circ, 90^\circ)$. The polycrystal is evolved using the thresholding algorithm with $\epsilon = 0.01, 0.006$ and 0.003 . **b)-d)** Closeups of an evolving triple junction (red box) clearly show that the dihedral angles converge to $(\Theta_1, \Theta_2, \Theta_3) = (134.56^\circ, 90.89^\circ, 134.56^\circ)$ predicted by the Herring angle condition (4.1), as ϵ converges to zero.

initial orientation distribution given by

$$\theta(\mathbf{x}, t = 0) = \begin{cases} \theta_2 & \text{if } x_2 \leq 0.25 \text{ or } x_2 > 0.75, \\ \theta_3 & \text{if } 0.25 < x_2 \leq 0.75 \text{ and } 0.25 \leq x_1 < 0.75, \\ \theta_1 & \text{if } 0.25 < x_2 \leq 0.75 \text{ and } x_1 > 0.25 \text{ or } x_1 > 0.75, \end{cases} \quad (4.2)$$

resulting in four triple junctions at $(x_1, x_2) = (0.25, 0.75), (0.75, 0.75), (0.75, 0.25)$, and $(0.25, 0.25)$. The initial dihedral angles of the triple junctions are $90^\circ, 180^\circ$, and 90° . Fig. 9a shows a plot of the initial orientation distribution of the tricrystal.

We begin by comparing the evolution of a triple junction predicted by the KWC model implemented using our thresholding scheme with that obtained using the Gaussian kernel method (Esedoglu and Otto, 2015). The grain boundary energies $(\gamma^{12}, \gamma^{23}, \gamma^{13}) = (0.62, 0.62, 87)$, pre-computed using the KWC model, are inputs to the Gaussian kernel method, and the respective mobilities are set to the inverse of the grain boundary energies. The parameter ϵ of the KWC model is taken as 0.01. Both schemes are simulated on a 1024×1024 grid. As shown

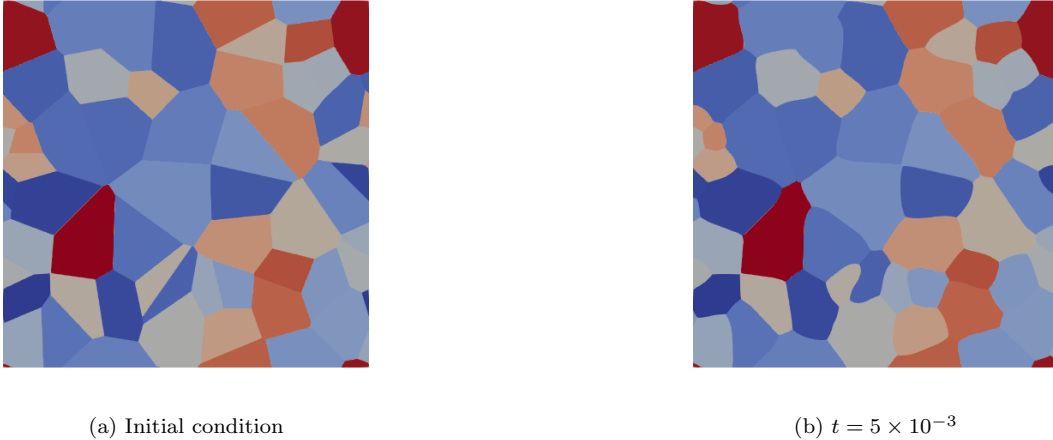


Figure 11: The ideal grain growth simulate by the current scheme. The constant core energy function $\mathcal{J}(\llbracket\theta\rrbracket) = 0.5$ results an isotropic grain boundary energy.

in Fig. 9, the evolution dynamics of both schemes are qualitatively similar. As expected, the triple junction adjusts at a faster time scale to satisfy the Herring angle condition compared to the curvature-driven motion of grain boundaries (Esedoglu et al., 2010). The motion of triple junctions induces a curvature in the grain boundaries, which drives the shrinking of the embedded grains (blue and yellow), while maintaining constant dihedral angles. The dihedral angles predicted by the Gaussian kernel method are $(93^\circ, 133.5^\circ, 133.5^\circ)$, while the generalized KWC model with $\epsilon = 0.01$ yields $(106^\circ, 127^\circ, 127^\circ)$.

To further investigate the dependence of the triple junction angles on ϵ , we implement the thresholding algorithm with $\epsilon = 0.01, 0.006$ and 0.003 on a 3000×3000 grid. As shown in Fig. 10b to Fig. 10d, as ϵ decreases, the stabilized triple junction angles converge to those predicted by the Herring relation. This test suggests that the Herring relation is satisfied in the limit $\epsilon \rightarrow 0$.

4.2. The Von Neumann-Mullins Theory of Grain Growth

In this section, we validate our thresholding scheme by testing the von Neumann–Mullins relation for a polycrystal with uniform grain boundary energies (γ) and mobilities (m). In two dimensions, the von Neumann-Mullins law (von Neumann, 1952; Mullins, 1956) states

$$\frac{dA}{dt} = \frac{\pi}{3} m \gamma (n - 6), \quad (4.3)$$

where A is the area of a grain with n sides, and γ . In other words, grains with more than six sides grow, while those with less than six sides will shrink.

To test the relation given in (4.3), we select the core energy function as a constant ($\mathcal{J}(\llbracket\theta\rrbracket) = 0.5$), and consider an initial polycrystal consisting of $\mathcal{N} = 50$ grains. The initial configuration, shown in Fig. 11a, is generated using a Voronoi tessellation of uniformly distributed random points. We implemented Algorithm 1 with parameters $\epsilon = 0.01$, $\mathbf{e} = 10^{-6}$, and $\xi = 0.05$, on a 1024×1024 grid.

As described in Section 4.1, the evolution of the polycrystal begins with the motion of triple junctions to attain the dihedral angles $(120^\circ, 120^\circ, 120^\circ)$ predicted by (4.1) for constant

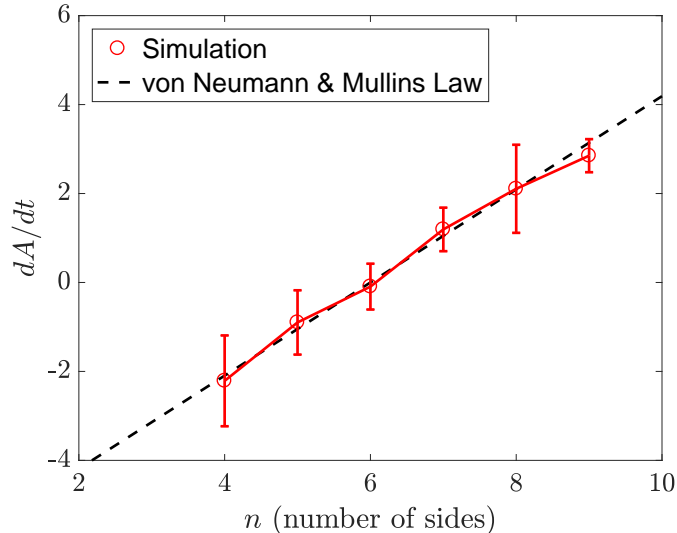


Figure 12: The mean and standard deviation of area change-rate for n -sided grain during the ideal grain growth shown in Fig. 11. The black dashed line $\dot{A}(n) = (\pi/3)n - 2\pi$ indicates the von Neumann-Mullins equation (4.3) with the unit reduced mobility $m\gamma = 1$.

γ . Subsequently, grain boundary motion by curvature follows. A snapshot of an evolving grain microstructure at $t = 5 \times 10^{-3}$, simulated using our thresholding scheme, is shown in Fig. 11b. In Fig. 12, we plot the mean rate of change of area of grains — along with standard deviation — measured during the time interval $[2.5 \times 10^{-3}, 5.0 \times 10^{-3}]$, as a function of the number of sides. Noting that the plot in red is close to the theoretically predicted black dashed line, we confirm that our thresholding scheme accurately predicts the von Neumann-Mullins law.

4.3. Comparison with the finite element implementation of the KWC model

In this section, we compare the evolutions of a polycrystal resulting from our thresholding method and a finite element implementation of the KWC model, which we will refer to as *FE-KWC*. An initial polycrystal consisting of $\mathcal{N} = 50$ grains, as shown in Fig. 13a, is generated using a Voronoi tessellation of uniformly distributed random points. The orientations of the grains are randomly chosen from the interval $[0, \pi/2]$. The core energy is chosen to be of the Read-Shockley-type, i.e. $\mathcal{J} = \llbracket \theta \rrbracket$.

The thresholding algorithm is implemented on a 1024×1024 grid, with parameters $\epsilon = 0.01$, $\mathbf{e} = 10^{-6}$, and $\xi = 0.05$. A snapshot of an evolving grain microstructure at $t = 5 \times 10^{-3}$, simulated using our thresholding scheme, is shown in Fig. 13b.

We note that FE-KWC, using continuous Lagrange finite elements, cannot be carried out on our model since the solution for θ is discontinuous. Therefore, we proceed with a finite element implementation of the regularized KWC model given in (2.4). We use second-order quadrilateral Lagrange finite elements to interpolate the order parameters. Since the regularized model allows grain rotation, we inhibit rotation using the following η -dependent mobility for θ

$$b_{\theta}^{-1}(\eta) = 10^{-5}\epsilon + (1 - \eta^3(10 - 15\eta + 6\eta^2))(1 - 10^{-5})\epsilon, \quad (4.4)$$

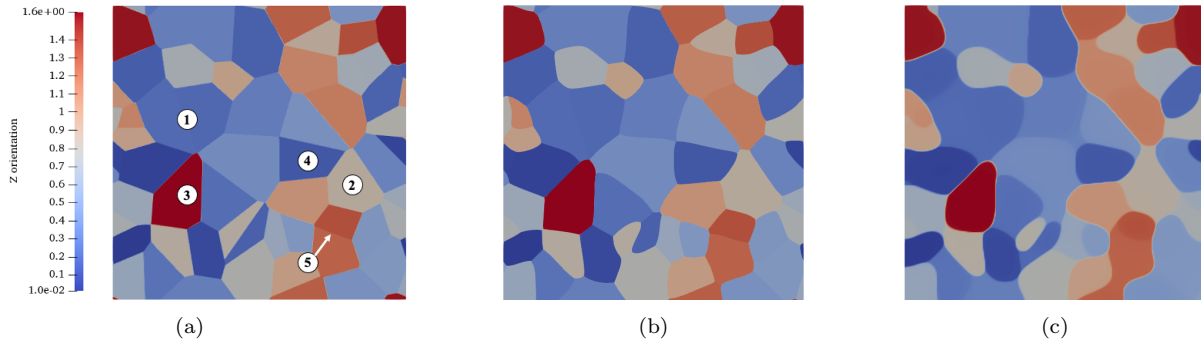


Figure 13: An initial polycrystal, shown in (a), is evolved using the thresholding and the finite element methods resulting in polycrystals shown in (b) and (c) respectively. The two methods are consistent in predicting the growth (e.g., ①, ②) and shrinkage (e.g., ③, ④) in various grains. The differences in the evolution is attributed to the mobility function introduced in (4.4) to prevent grain rotation.

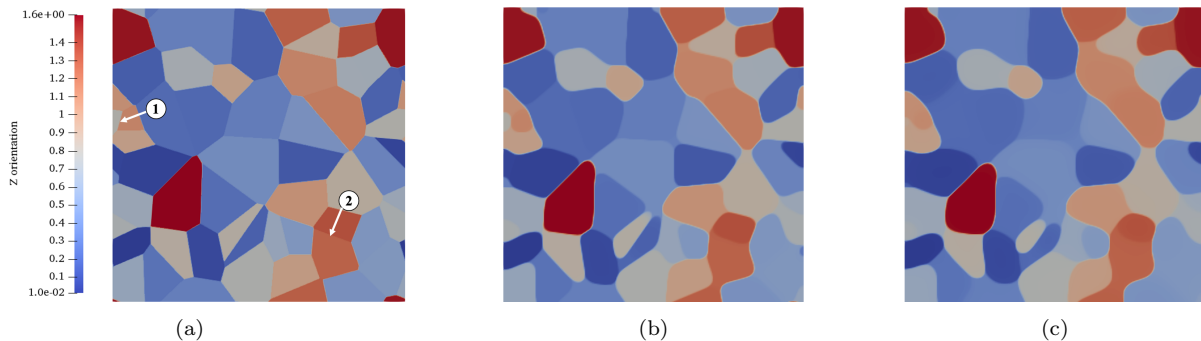


Figure 14: An initial polycrystal, shown in (a), is evolved using the finite element method. (b) and (c) show the resulting polycrystals with regularization parameters $\rho_0 = 2 \times 10^{-4}$ and $\rho_0 = 2 \times 10^{-3}$ respectively. When ρ_0 is not sufficiently small, grains with small misorientation (e.g., ①, ②) blend out and grain boundaries easily become rounded. However, the decrease in ρ_0 for simulating sharp interfaces, comes with significant computational cost contrasts to the suggested scheme.

as suggested by [Dorr et al. \(2010\)](#). On the other hand, $(b_\eta)^{-1} = \epsilon$ is chosen to be constant. To address the singularity due to the $|\nabla\theta|$ term in (2.4b), we use the approximation

$$g(\eta)|\nabla\theta| \approx g(\eta)\sqrt{\rho_0 + |\nabla\theta|^2}, \quad (4.5)$$

where $\rho_0 = 2 \times 10^{-3}$ is a constant. The manifestation of ρ_0 on the solution will be discussed below. FE-KWC is performed on the open-source computing platform [Fenics Alnaes et al. \(2015\)](#). We take an implicit time step with $dt = 0.012$. In order to compare the numerical efficiency, we ensure that the number of degrees of freedom is the same in the thresholding and the finite element simulations. The grain microstructure at $t = 1.71$, simulated using FE-KWC, is shown in Fig. 13c.

Comparing Figs. 13b–13c, we note that both the methods are consistent in predicting growth (see ①, ②) and shrinkage (see ③, ④) in various grains. It is observed that grain boundaries become rounded in the finite element simulation, because of the diffusive nature of orientation field. In addition, disparities are more clear for small misorientation grain

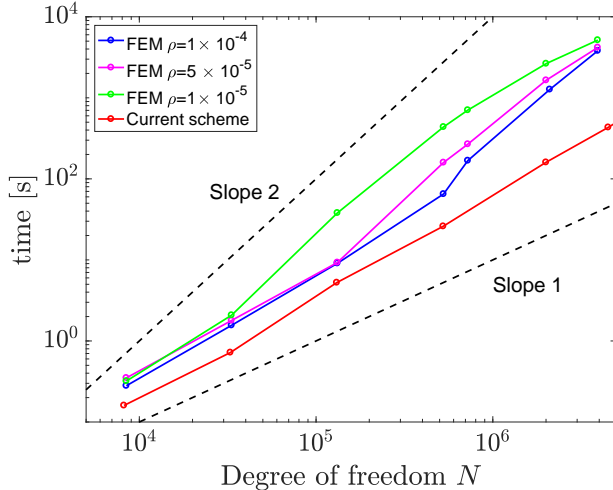


Figure 15: A comparison of the complexity of the thresholding and the finite element methods. The dashed lines represent reference slopes in the log-log scale plot. Slope 1 and 2 represent $\mathcal{O}(N)$ and $\mathcal{O}(\log N)$ respectively. While both methods have a complexity of at most $\mathcal{O}(N \log N)$, the cost of the finite element method depends on the choice of ρ .

boundaries, e.g. ⑤, which are highly diffused. This is a manifestation of ρ_0 , which results in a non-zero gradient in θ in the grain interiors. In Fig. 14, we compare two finite element simulations with $\rho_0 = 2 \times 10^{-3}$ and 2×10^{-4} , which shows that for a smaller ρ_0 , the grain boundaries retain their characteristic width.¹³ Thus, to simulate sharp grain interfaces comparable to the our scheme, a small enough ρ_0 is required for FE-KWC. However, we note that the decrease in ρ_0 increases the stiffness of the equations, which significantly affects the computational time as discussed below.

Computational time study clearly highlights the advantage of the our thresholding scheme. Performance tasks are executed on a single 1.6 GHz core with 8 GB RAM, and we measured the wall-clock time to complete one-full time step for the two methods. For our method, this includes solving for η using the primal dual algorithm, and executing the fast marching based thresholding algorithm to update θ . In Fig. 15, we plot the dependence of the wall-clock time, as a function of the number of degrees of freedom N . The computational complexity of the current scheme is $\mathcal{O}(N \log N)$, with a dominant contribution from FFT used in the primal dual algorithm to solve (C.7). On the other hand, the asymptotic computational cost of FE-KWC is estimated to be in between $\mathcal{O}(N)$ and $\mathcal{O}(N^2)$ as shown in Fig. 15. The computational bottleneck of FE-KWC is in solving — using a GMRES iterative solver (Saad and Schultz, 1986) — a linear system of equations formed by an $N \times N$ -sized sparse matrix. Though the asymptotic costs of the two schemes are similar in terms of N , we note that the computational cost of FE-KWC also depends on the choice of the regularization parameter ρ_0 , which increases the stiffness of the equations in the limit $\rho \rightarrow 0$. Therefore, as demonstrated in Fig. 15, the current scheme can be orders of magnitude faster than FE-KWC. Both, FE-KWC

¹³Recall that the characteristic width of a grain boundary in the regularized KWC model is a function of ϵ .

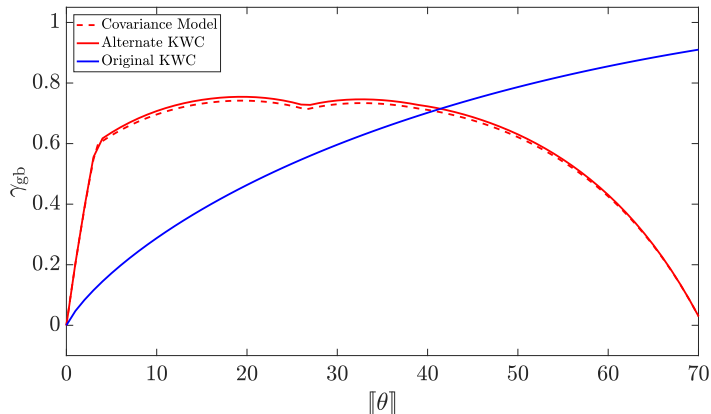


Figure 16: Grain boundary energies used for the polycrystal simulation in Section 4.4. Using a core energy $\mathcal{J}(\llbracket\theta\rrbracket)$ designed in Section 2.2, we obtain a crystal symmetry-invariant KWC model with energy that matches the covariance model. In order to compare the original and the new KWC models, we scale the function g of the original KWC model in (2.1) to $g = -0.93 \ln(1 - \eta)$ such that the averages of the grain boundary energies (with respect to misorientation) are identical in the two models. In other words, the areas under the above plots are equal.

and the implementation of our method, can be well-parallelized using the current generation of graphics cards, which have the power, programmability and precision to implement FFT and iterative matrix solvers (Li and Saad, 2013; Govindaraju et al., 2008) respectively.

4.4. Grain growth in an fcc copper polycrystal

In this section, we examine grain growth in a two-dimensional fcc copper polycrystal with $[110]$ -type grain boundaries simulated using the generalized KWC model,¹⁴ with crystal symmetry-invariant grain boundary energy. We compare the results with the predictions of the original KWC model.

A two-dimensional polycrystal consisting of $\mathcal{N} = 50$ grains, with orientations in the range $[0, 70.6^\circ]$ is generated using a Voronoi tessellation of random points. Fig. 17 shows the initial orientation distribution in the polycrystal. We assume that the grain boundary energy density is independent of inclination. We use the core energy $\mathcal{J}(\llbracket\theta\rrbracket)$ constructed in Section 2.2 (see Fig. 3). In order to compare the generalized model to the original KWC model, we scale the function g of the original KWC model in (2.1) to $g = -0.93 \ln(1 - \eta)$ such that the mean of the grain boundary energies as functions of misorientation in the range $[0, 70.6^\circ]$ are identical for the two models. Fig. 16 shows a comparison of the grain boundary energy densities of the two models.

The orientation distributions of the polycrystal at the end of 200 time steps for the generalized and the original KWC models are shown in Figs. 17b–17c respectively. Comparing the resulting polycrystals with the initial polycrystal in Fig. 17a, we note that the generalized KWC model predicts a growth for red grains while the original model results in their shrinkage. This can be attributed to the difference in the grain boundary energies of the two

¹⁴The $[110]$ direction of each grain is aligned with the z -axis (out of the plane).

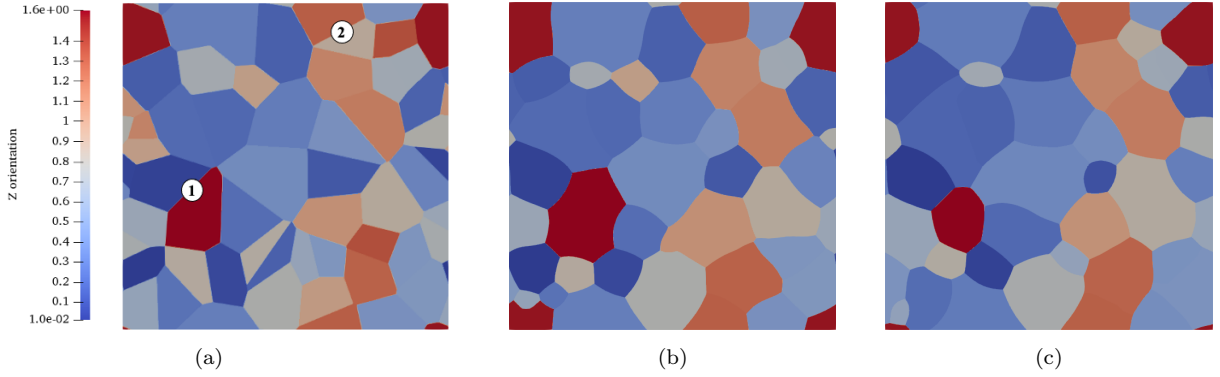


Figure 17: (a) A polycrystal with $\mathcal{N} = 50$ grains, and an initial orientation distribution. (b) and (c) show evolved polycrystals using the new and the original KWC models respectively. Grains 1 and 2 show opposite growth/shrinkage trends in the two models due to the deviation of the grain boundary energy from the Read–Shockley-type in the new formulation. The blue and red colors represent the maximum and minimum orientation angles of 0° and 70.6° respectively.

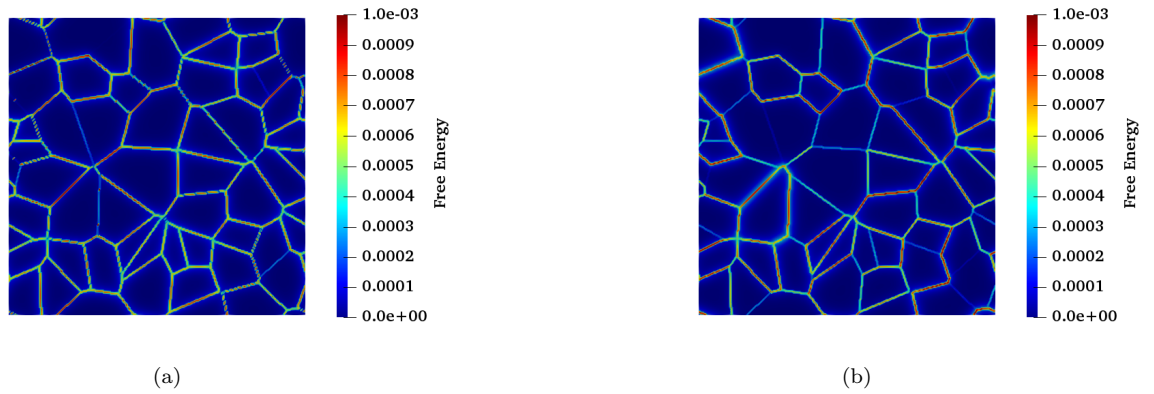


Figure 18: Initial distributions of grain boundary energies for the (a) generalized, and (b) the original KWC models. The grain boundary energy in the original KWC model is of the Read–Shockley-type. On the other hand, the grain boundary energy in the generalized KWC model reflects the crystal symmetry of copper.

models, as shown in Fig. 18. For example, the grain boundary ①, which has a misorientation of $\approx 70.6^\circ$ has a relatively smaller energy in the generalized model due to crystal symmetry.

On the other hand, we note an opposite trend for light blue grains for which the generalized model predicts shrinkage while the original model results in a growth. This is a result of relatively larger energy of grain boundary ② in the generalized model compared to the original model. The above observations suggest that the generalized model can result in the growth of certain grains with large misorientation, highlighting the importance of crystallography in grain growth.

5. Conclusion and future work

In this work, we generalized the two-dimensional KWC model for grain boundaries such that it can incorporate arbitrary misorientation-dependent grain boundary energies that respect the bicrystallography of grain boundaries. In addition, we address the computational challenge of solving a singular diffusive equation of the KWC model by developing an $\mathcal{O}(N \log N)$ thresholding algorithm. Below, we summarize the construction of our model, its implementation, and research directions for future work.

First, we eliminate the $|\nabla\theta|^2$ term in the original KWC model, which is responsible for regularizing the orientation order parameter, and rendering a non-zero mobility to the grain boundaries. The lack of a regularizing term results in a discontinuous orientation order parameter with jump across the grain boundaries, and grain boundaries with no mobility. In the presence of a piecewise-constant orientation order parameter, the modified KWC functional can be separated into a bulk contribution that depends on η , and a surface contribution, called the core energy, that depends linearly on the jump $[[\theta]]$ across the grain boundaries. Next, we show that by generalizing the core energy from a linear function to an arbitrary function \mathcal{J} of $[[\theta]]$, the model can incorporate arbitrary dependence of grain boundary energies on misorientation angles.

Since the absence of the regularizing $|\nabla\theta|^2$ term renders the grain boundaries immobile, we design an $\mathcal{O}(N \log N)$ thresholding algorithm to evolve grain boundaries by curvature, where N is the number of grid points. The algorithm, which employs a primal-dual and the fast marching methods, is shown to be an order of magnitude faster than the finite element implementation of the original KWC model. We validate our implementation by predicting the Herring angle relation, and simulate a two-dimensional polycrystal consisting of [110] tilt grain boundaries. The computational efficiency and flexibility of our approach opens the door to a number of exiting directions for future work.

- The present framework will enable us to carry out a statistical study of large scale simulations of various ensembles of polycrystals to characterize abnormal grain growth in terms of the grain boundary energy landscape and crystal symmetry.
- While arbitrary grain boundary energies can be incorporated into our model, its implementation is restricted to grain boundary mobility equal to the inverse of the energy. An extension of our algorithm to include mobilities independently will be explored in a future work.

- The present algorithm does not allow grain rotation, which is another important phenomenon during recrystallization of polycrystalline materials.¹⁵ We plan to augment the current scheme with a step that models grain rotation.
- A recent work by [Admal et al. \(2019\)](#) extended the two-dimensional KWC model to a three-dimensional fully anisotropic (both misorientation and inclination dependent) model, wherein the dependence of grain boundary energy on the misorientation angle was restrictive to a Read–Shockley-type. Due to the high computational cost of the finite element method, the implementation of the three-dimensional model was restricted to simple bicrystals. It is envisaged that the efficiency of our thresholding algorithm will enable us to explore large three-dimensional polycrystals with fully anisotropic grain boundary energy.
- Finally, we recall from the introduction that surface tension is not the only dominant driving force on a grain boundary due to grain boundary plasticity. Adapting our thresholding algorithm into existing unified frameworks ([Admal et al., 2018](#)), wherein grain microstructure and deformation evolve contemporaneously, will enable us to quantify the role of grain boundary plasticity, and study phenomena such as dynamic recrystallization, superplasticity and severe plastic deformation ([Thomas et al., 2017](#); [Wei et al., 2020](#); [Runnels and Agrawal, 2020](#)).

Data availability

A C++ template library that implements Algorithm 1 is available at <https://github.com/admal-research-group/GBthresholding>.

CRedit author statement

Jaekwang Kim: Formal analysis, Investigation, Software, Validation, Writing-Original draft, Visualization. **Matt Jacobs:** Conceptualization, Methodology, Software, Formal analysis. **Stanley Osher:** Conceptualization. **Nikhil Admal:** Conceptualization, Methodology, Writing-Review and Editing, Resources, Data Curation, Supervision, Project Management.

Appendix A. Results on the 1D KWC model

In this section, we collect results on the one-dimensional KWC model which describes an infinite bicrystal with a grain boundary at the origin. In particular, we present the derivation

¹⁵We note that grain rotation may sometimes play an important role during the transition from recovery to continuous dynamic recrystallization. Dislocations agglomerate and form cell walls/subgrains at the end of the recovery stage. In a phenomenon, commonly referred to as *subgrain rotation recrystallization*, few subgrains — aided by bulk dislocations — increase their misorientation and transform to grains/nuclei which grow ([Li, 1962](#)). From this perspective, grain rotation plays an important role during the nucleation of recrystallized grains.

of the steady-state analytical solution under Dirichlet boundary conditions, and the resulting grain boundary energy as a function of misorientation.

Consider the following KWC energy functional without the $|\nabla\theta|^2$ regularizing term

$$\mathcal{W}[\eta, \theta] = \int_{-\infty}^{\infty} \left[\frac{\epsilon}{2} |\nabla\eta|^2 + \frac{(1-\eta)^2}{2\epsilon} + g(\eta) |\nabla\theta| \right] dV. \quad (\text{A.1})$$

The Euler–Lagrange equation associated with the above functional is

$$\epsilon\Delta\eta - \frac{\eta-1}{\epsilon} - g_{,\eta} |\nabla\theta| = 0, \quad (\text{A.2})$$

where $g_{,\eta}$ is used to denote $\partial g/\partial\eta$. In what follows, we derive a steady-state solution of (A.2) under Dirichlet boundary conditions

$$\eta(\pm\infty) = 1, \quad \theta(\infty) = -\theta(-\infty) = \theta/2. \quad (\text{A.3})$$

We begin with the ansatz that $\theta(x)$ is a step function satisfying (A.3) with a discontinuity at the origin. Multiplying (A.2) by η' , and integrating with respect to x in a region away from the origin, we obtain

$$\frac{\epsilon}{2} \eta_{,x}^2 - \frac{(1-\eta)^2}{2\epsilon} = 0, \implies \eta_{,x} = \pm \frac{(1-\eta)}{\epsilon}, \quad (\text{A.4})$$

On the other hand, multiplying (A.2) with η' , and integrating over an arbitrarily small neighborhood of 0 results in the jump condition

$$\epsilon[[\eta_{,x}]] = g_{,\eta}(\bar{\eta})[[\theta]], \quad (\text{A.5})$$

where $\bar{\eta} := \eta(0)$ is the value of η at the grain boundary. From (A.4) and (A.5), it follows that

$$\epsilon\eta_{,x} = \begin{cases} 1-\eta & \text{if } x > 0, \\ -(1-\eta) & \text{otherwise,} \end{cases} \quad (\text{A.6})$$

and

$$g_{,\eta}(\bar{\eta})[[\theta]] = 2(1-\eta), \quad (\text{A.7})$$

which relates $\bar{\eta}$ to $[[\theta]]$. The analytical solution for η can be obtained by integrating (A.4). With our choice of $g = -\ln(1-\eta)$, the result can be explicitly written as a function of misorientation $[[\theta]]$:

$$\int_{\bar{\eta}}^{\eta} \frac{\epsilon}{1-\eta} d\eta = x, \implies \eta(x) = 1 - \sqrt{\frac{[[\theta]]}{2}} \exp\left(-\frac{|x|}{\epsilon}\right). \quad (\text{A.8})$$

The grain boundary energy γ as a function of misorientation is calculated by evaluating

$\mathcal{W}[\eta, \theta]$ using the steady state solution for η derived above. From (A.4), we have

$$\begin{aligned}\gamma(\llbracket\theta\rrbracket) &= \mathcal{W}[\eta, \theta] = \int_{-\infty}^{\infty} \left[\frac{\epsilon}{2} \eta_{,x}^2 + \frac{(1-\eta)^2}{2\epsilon} \right] dx + g(\bar{\eta}) \llbracket\theta\rrbracket \\ &= 2 \int_0^{\infty} \frac{(1-\eta)^2}{\epsilon} dx + g(\bar{\eta}) \llbracket\theta\rrbracket \\ &= 2 \int_{\bar{\eta}}^1 (1-\eta) d\eta + g(\bar{\eta}) \llbracket\theta\rrbracket = (1-\bar{\eta})^2 + g(\bar{\eta}) \llbracket\theta\rrbracket.\end{aligned}\quad (\text{A.9})$$

Note that the grain boundary energy γ and $\bar{\eta}$ are independent of ϵ , which reinforces that the model converges to its sharp interface as $\epsilon \rightarrow 0$ while the energy remains unchanged. Again specializing the analytical expression γ with the choice of the logarithmic g , we obtain

$$\begin{aligned}\gamma(\llbracket\theta\rrbracket) &= (1-\bar{\eta})^2 - \llbracket\theta\rrbracket \ln(1-\bar{\eta}) \\ &= \frac{\llbracket\theta\rrbracket}{2} - \llbracket\theta\rrbracket \ln \left(\sqrt{\frac{\llbracket\theta\rrbracket}{2}} \right).\end{aligned}\quad (\text{A.10})$$

Appendix B. The covariance model of grain boundary energy

The covariance model for grain boundary energy, developed by [Runnels et al. \(2016a,b\)](#), estimates grain boundary energy using the covariance of atomic densities of the two lattices adjoining a grain boundary.

In the covariance model, a lattice density measure $\bar{\rho}$ for a given lattice¹⁶ \mathcal{L} , defined as an infinite sum of Dirac measures with support at the lattice points of \mathcal{L} :

$$\bar{\rho}(\mathbf{x}) = \sum_{\mathbf{d} \in \mathcal{L}} \delta(\mathbf{x} - \mathbf{d}). \quad (\text{B.2})$$

A lattice density field ρ is introduced as the convolution of $\bar{\rho}$ with a thermalization function ξ , i.e.

$$\rho(\mathbf{x}) = \bar{\rho}(\mathbf{x}) * \xi(\mathbf{x}), \quad (\text{B.3})$$

where

$$\xi(\mathbf{x}) = \frac{1}{\sigma^3 \pi^{3/2}} e^{-\|\mathbf{x}\|^2 / \sigma^2}, \quad (\text{B.4})$$

with σ^2 as the dimensionless temperature. The planar covariance of two thermalized lattices \mathcal{L}_A and \mathcal{L}_B with their respective density fields ρ_A and ρ_B , measured on \mathbb{R}^2 , is defined as

$$c[\rho_A, \rho_B] = \int_{\mathbf{y} \in \mathbb{R}^2} \rho_A(P^T \mathbf{y}) \rho_B(P^T \mathbf{y}) \lambda(\mathbf{y}) dA, \quad (\text{B.5})$$

¹⁶A lattice \mathcal{L} is defined using three lattice vectors \mathbf{l}_1 , \mathbf{l}_2 , and \mathbf{l}_3 as

$$\mathcal{L} = \{n_1 \mathbf{l}_1 + n_2 \mathbf{l}_2 + n_3 \mathbf{l}_3 \mid n_i \in \mathbb{Z}\}. \quad (\text{B.1})$$

where $\lambda(\mathbf{x})$ is an appropriately chosen window function (see (B.8), $P : \mathbb{R}^3 \rightarrow \mathbb{R}^2$ is the projection

$$P = \begin{pmatrix} 1 & 0 & 0 \\ 0 & 1 & 0 \end{pmatrix} \quad (\text{B.6})$$

on to the plane \mathbb{R}^2 . Expressing the functions ρ_A and ρ_B in Fourier series, the integral in (B.5) simplifies as

$$c[\rho_A, \rho_B] = \frac{1}{\hat{\lambda}(\mathbf{0})} \sum_{\mathbf{k}_A \in \mathcal{L}'_A} \sum_{\mathbf{k}_B \in \mathcal{L}'_B} \hat{\rho}(\mathbf{k}_A) \hat{\rho}^*(\mathbf{k}_B) \hat{\lambda}(P(\mathbf{k}_B - \mathbf{k}_A)), \quad (\text{B.7})$$

where \mathbf{k}_A and \mathbf{k}_B are lattice vectors of the dual lattices \mathcal{L}'_A and \mathcal{L}'_B , and the window function is defined in terms of its Fourier transform as

$$\hat{\lambda}(\mathbf{k}) = e^{-\|\mathbf{k}\|/\omega}, \quad (\text{B.8})$$

with an adjustable parameter ω . The grain boundary energy in the covariance model is defined as

$$\gamma^{\text{cov}} = E_0 \left(1 - \frac{c[\rho^A, \rho^B]}{c_{\text{gs}}} \right), \quad (\text{B.9})$$

where c_{gs} is the ground state covariance defined as the supremum, over all planes, of $c[\rho_A, \rho_A]$. For example, in fcc, c_{gs} corresponds to covariance measured with respect to the [111] plane. Finally, we note that the covariance model has three adjustable parameters $\{E_0, \sigma, \omega\}$ that can be used to fit γ^{cov} to data from experiments or molecular dynamics simulations. It is known that while (B.9) is a good indicator of grain boundary energy, it over-predicts the energy for low angle grain boundaries as the above model does not account for facet formation. [Runnels et al. \(2016a,b\)](#) have shown that a further relaxation of the grain boundary energy, which signifies the formation of facets, yields necessary corrections to the energy predicted by the model.

Fig. B.19 shows a plot of a relaxed γ^{cov} computed for [110] symmetric-tilt grain boundaries in fcc copper using $E_0 = 1.45 \text{ J/m}^{-2}$, $\omega = 0.5$, and $\sigma/a_0 = 0.175$, where $a_0 = 3.597$ is the lattice constant of copper. From Fig. B.19, it is clear that the grain boundary energy predicted by the covariance model is in good overall agreement with data from molecular dynamics simulations ([Wolf, 1990](#); [Miura et al., 1994](#)).

Appendix C. The primal-dual method

Primal-dual methods is a part of a class of first-order algorithms¹⁷ that have a long history in the context of optimization problems ([Powell, 1978](#); [Kuhn, 1955](#); [Komodakis and Pesquet, 2015](#)). As the name suggests, primal-dual methods proceed by concurrently solving a primal problem and a dual problem. The main benefit of primal-dual splitting is that it replaces an original hard problem with a set of two easy sub-problems (primal- and dual-). Because of this advantage, the method has been widely used in diverse fields including compressed

¹⁷An algorithm that only requires the calculation of the gradient of a functional.

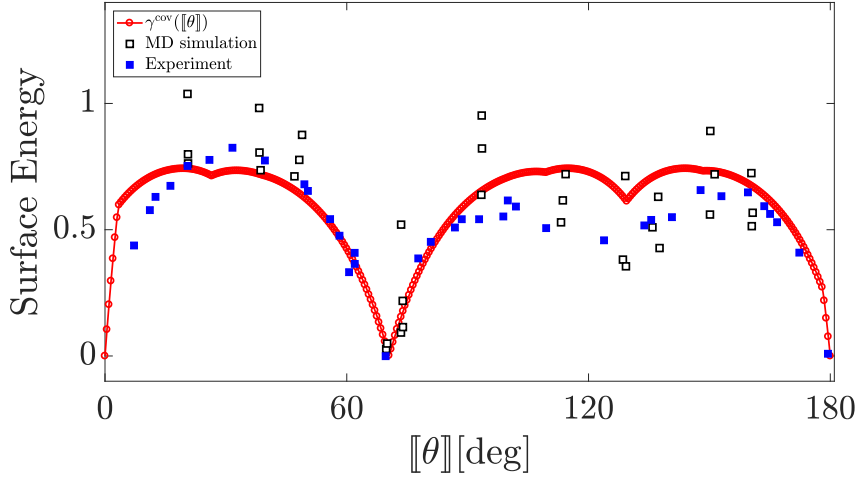


Figure B.19: A plot of the normalized grain boundary energy versus the misorientation angle predicted by the covariance model for a [110] symmetric-tilt grain boundary in fcc copper, computed using the relaxation algorithm of [Runnels et al. \(2016a,b\)](#). For comparison, grain boundary energies obtained from experiment ([Miura et al., 1994](#)), and MD simulations ([Wolf, 1990](#)) are shown in blue and square points respectively.

sensing, image processing, signal processing, and machine learning ([Donoho, 2006](#); [Chambolle and Pock, 2011](#); [Shalev-Shwartz and Singer, 2007](#); [Combettes and Pesquet, 2011](#)).

The motivation to use a primal-dual algorithm to solve the minimization problem in (3.1) for η arises due to the presence of a highly nonlinear term $g(\eta)\mathcal{J}([\theta])$ along with $|\nabla\eta|^2$. Therefore, we adopt a primal-dual method by introducing an auxiliary dual variable which enables us to cast (3.1) as an equivalent optimization problem. The choice of the dual variable is based on the observation that

$$\begin{aligned} \frac{\epsilon}{2}\|\nabla\eta\|_{L^2(\Omega)}^2 &= \epsilon\|\nabla\eta\|_{L^2(\Omega)}^2 - \frac{\epsilon}{2}\|\nabla\eta\|_{L^2(\Omega)}^2 \\ &= -\epsilon\int_{\Omega}\eta\Delta\eta dV - \int_{\Omega}\frac{\epsilon}{2}\nabla\eta\cdot\nabla\eta dV, \end{aligned} \quad (\text{C.1})$$

where we have used the divergence theorem, and the Neumann boundary condition $\nabla\eta\cdot\mathbf{n} = \mathbf{0}$. Introducing an auxiliary variable ψ , and identifying it with $-\epsilon\Delta\eta$, we have

$$\begin{aligned} \frac{\epsilon}{2}\|\nabla\eta\|^2 &= \sup_{\psi\in(\dot{H}^1(\Omega))^*} \left[\int_{\Omega}\eta(x)\psi(x) dV - \frac{1}{2\epsilon}\|\Delta^{-1}\nabla\psi\|_{L^2(\Omega)}^2 \right] \\ &= \sup_{\psi\in(\dot{H}^1(\Omega))^*} \left[\int_{\Omega}\eta(x)\psi(x) dV - \frac{1}{2\epsilon}\|\psi\|_{(\dot{H}^1(\Omega))^*}^2 \right], \end{aligned} \quad (\text{C.2})$$

where $\dot{H}^1(\Omega)$ denotes the set of all functions in $H^1(\Omega)$ with zero average, and $(\dot{H}^1(\Omega))^*$ is its dual. Substituting (C.2) into the KWC functional \mathcal{W}^G , the minimization problem in (3.1)

transforms to the following saddle point problem:

$$\inf_{\eta \in L^2(\Omega)} \sup_{\psi \in (\dot{H}^1(\Omega))^*} \Phi[\eta, \psi], \quad (\text{C.3})$$

where

$$\Phi[\eta, \psi] = -\frac{1}{2\epsilon} \|\psi\|_{(\dot{H}^1(\Omega))^*}^2 + \int_{\Omega} (\eta\psi + f(\eta)) dV + \int_{\mathcal{S}} g(\eta) \mathcal{J}([\theta]) dS. \quad (\text{C.4})$$

The problems of minimizing Φ with respect to η , and maximizing it with respect to ψ are referred to as η and ψ sub-problems respectively. The advantage of using a primal-dual algorithm is evident from the observation that Ψ *does not* depend on the gradients of η , which renders the η sub-problem local, and the nonlinearity in $g(\eta)$ is no longer a concern. The existence and uniqueness of solutions to the sub-problems follows from standard convex analysis.

We solve for the saddle point of Φ using the following primal-dual update scheme (Algorithm 2 in (Chambolle and Pock, 2011)):

$$\eta_{n+1} = \arg \min_{\eta \in L^2(\Omega)} \left[\Phi(\eta, \psi_n) + \frac{1}{2\tau_n} \|\eta - \eta_n\|_{L^2(\Omega)}^2 \right], \quad (\text{C.5a})$$

$$\psi_{n+1} = \arg \max_{\psi \in (\dot{H}^1(\Omega))^*} \left[\Phi(\tilde{\eta}_{n+1}, \psi) - \frac{1}{2\sigma_n} \|\psi - \psi_n\|_{L^2(\Omega)}^2 \right], \quad (\text{C.5b})$$

where

$$\tilde{\eta}_{n+1} = (1 + \mu_n)\eta_{n+1} - \mu_n\eta_n$$

with

$$\mu_n = 1/\sqrt{1 + 2\tau_n/\epsilon}, \quad \tau_{n+1} = \mu_n\tau_n, \quad \sigma_{n+1} = \sigma_n/\mu_n.$$

The scalars τ_n and σ_n are the step sizes of the η - and ψ -update respectively. The stability (Jacobs et al., 2019; Chambolle and Pock, 2011) of the update scheme in (C.5) is guaranteed if $\tau_n\sigma_n \leq 1$. We select $\tau_0 = \epsilon, \sigma_0 = 1/\epsilon$. The solution to (C.5) is obtained by solving the following Euler–Lagrange equations corresponding to gradient flows of the two functionals in (C.5) ¹⁸

$$\left(\frac{1}{\epsilon} + \frac{1}{\tau_n} \right) \eta^2(x) + \left(\psi_n(x) - \frac{2}{\epsilon} - (1 + \eta_n) \frac{1}{\tau_n} \right) \eta(x) - \mathcal{J}^*([\theta]) + \frac{1}{\epsilon} - \psi_n + \frac{1}{\tau_n} \eta_n = 0, \quad (\text{C.6})$$

$$(1/\epsilon - \Delta/\sigma_{n+1})\psi_{n+1} = -\Delta(\tilde{\eta}_{n+1} + \psi_n/\sigma_{n+1}), \quad (\text{C.7})$$

where the surface measure $\mathcal{J}([\theta]) dS$ has been replaced by a volume measure $\mathcal{J}^* dV = \mathcal{J}([\theta]) \exp(-x^2/2\epsilon^4) dV$ that depends on the distance x from the grain boundary. From (C.6), we note that the primal dual algorithm along with the choice $g(\eta) = -\log(1 - \eta)$ not only renders the η sub-problem local but also analytically solvable.

We solve (C.6) and (C.7) on a uniform grid of size $N = N_x \times N_y$. Since (C.6) is solved

¹⁸In order to obtain (C.7), we note that the constrained gradient in $(\dot{H}^1(\Omega))^*$ of $\int_{\Omega} \tilde{\eta}_{n+1} \psi dV$ with respect to ψ is $-\Delta \tilde{\eta}_{n+1}$.

analytically at each grid point, its cost remains $\mathcal{O}(N)$. We solve for ψ_{n+1} in (C.7) using the fast Fourier transform (FFT), resulting in an $\mathcal{O}(N \log N)$ complexity for the primal dual algorithm. We use the following stopping criterion for the update scheme in (C.5),

$$\|\eta_{n+1} - \eta_n\|_\infty = \max_{1 \leq j \leq N} |(\eta_{n+1})_j - (\eta_n)_j| \leq \mathbf{e}, \quad (\text{C.8})$$

where \mathbf{e} is the tolerance of the iterative scheme. Finally, we note that the use of FFT to solve (C.7) necessitates periodic boundary conditions on η . On the other hand, for Neumann boundary conditions, we use the discrete cosine transform given by

$$\hat{\psi}_{pq} = \lambda_p \lambda_q \sum_{i=0}^{N_x-1} \sum_{j=0}^{N_y-1} \psi \left(\frac{i}{N_x}, \frac{j}{N_y} \right) \cos \left(\frac{\pi(2i+1)p}{2N_x} \right) \cos \left(\frac{\pi(2j+1)q}{2N_y} \right), \quad \begin{array}{l} 0 \leq p \leq N_x - 1 \\ 0 \leq q \leq N_y - 1, \end{array} \quad (\text{C.9})$$

with

$$\lambda_p = \begin{cases} 1/\sqrt{N_x}, & p = 0, \\ \sqrt{2/N_x}, & 1 \leq p \leq N_x - 1, \end{cases} \quad \text{and} \quad \lambda_q = \begin{cases} 1/\sqrt{N_y}, & q = 0, \\ \sqrt{2/N_y}, & 1 \leq q \leq N_y - 1. \end{cases} \quad (\text{C.10})$$

Appendix D. Note on the derivations of thresholding scheme

In this section, we describe the steps to obtain (3.8) from (3.7). We begin by separating the domain of integration in (3.7) as

$$\int_{-\infty}^{l_0} (1 - u(l/\epsilon))^2 dl = \int_{l_0}^0 (1 - u(l/\epsilon))^2 dl + \int_0^{+\infty} (1 - u(l/\epsilon))^2 dl. \quad (\text{D.1})$$

Substituting the solution in (3.6) into (D.1), we have

$$\frac{(u(0) - 1)^2}{\left(\frac{2}{\epsilon} - \kappa\right)} \exp \left[\left(\frac{2}{\epsilon} - \kappa \right) l_0 \right] = \frac{(u(0) - 1)^2}{\left(\frac{2}{\epsilon} - \kappa\right)} \left(1 - \exp \left[\left(\frac{2}{\epsilon} - \kappa \right) l_0 \right] \right) + \frac{(u(0) - 1)^2}{\left(\frac{2}{\epsilon} + \kappa\right)}. \quad (\text{D.2})$$

Dividing both sides by $(u(0) - 1)^2$ and collecting the l_0 terms, we obtain

$$\frac{2 \exp \left[\left(\frac{2}{\epsilon} - \kappa \right) l_0 \right]}{\left(\frac{2}{\epsilon} - \kappa\right)} = \frac{1}{\left(\frac{2}{\epsilon} - \kappa\right)} + \frac{1}{\left(\frac{2}{\epsilon} + \kappa\right)} = \frac{\frac{4}{\epsilon}}{\left(\frac{4}{\epsilon^2} - \kappa^2\right)}. \quad (\text{D.3})$$

Taking a logarithm, we have

$$\left(\frac{2}{\epsilon} - \kappa \right) l_0 = \log \left(\frac{2/\epsilon}{2/\epsilon + \kappa} \right) = \log \left(\frac{1}{1 + (\epsilon\kappa)/2} \right). \quad (\text{D.4})$$

A Taylor expansion of the right-hand-side of (D.4) with respect to $\epsilon\kappa/2$ results in

$$\left(\frac{2}{\epsilon} - \kappa \right) l_0 = -\frac{\epsilon\kappa}{2} + \frac{\epsilon^2\kappa^2}{4} - \frac{\epsilon^3\kappa^3}{8} + \mathcal{O}(\epsilon^4\kappa^4). \quad (\text{D.5})$$

Multiplying by ϵ on both sides, we have

$$(2 - \kappa\epsilon) l_0 = -\frac{\epsilon^2 \kappa}{2} + \frac{\epsilon^3 \kappa^2}{4} + \frac{\epsilon^4 \kappa^3}{8} + O(\epsilon^4 \kappa^4). \quad (\text{D.6})$$

Finally, using the approximation $2 - \kappa\epsilon \approx 2$, we get (3.8).

As mentioned in Section 3.2, in practice, the infinite bounds of the integral in (D.1) are replaced by finite bounds of magnitude l_b . Under this change, (D.6) modifies as

$$\left(\frac{2}{\epsilon} - \kappa\right) l_0 = \log \left(\frac{\frac{2}{\epsilon}}{\frac{2}{\epsilon} + \kappa} + \boxed{\frac{1}{2} \exp \left(- \left(\frac{2}{\epsilon} - \kappa \right) l_b \right) - \frac{\left(\frac{2}{\epsilon} - \kappa \right)}{2 \left(\frac{2}{\epsilon} + \kappa \right)} \exp \left(- \left(\frac{2}{\epsilon} + \kappa \right) l_b \right)} \right). \quad (\text{D.7})$$

It can be easily shown that the boxed terms resulting from a finite value of d_b decay exponentially as $\epsilon \rightarrow 0$, which leaves (3.8) unchanged.

Appendix E. Fast marching method

The fast marching method (FMM), developed by Tsitsiklis (1995) is used to evolve a surface in the outward unit normal direction with a speed $V(\mathbf{x}) > 0$. The fast marching method reformulates a time-dependent initial value problem describing the evolution of a surface into an equivalent boundary value formulation. In this section, we summarize the FMM algorithm as described in Sethian (1996). For illustration, let $\mathbf{s}(t)$ describe a surface evolving with speed \mathcal{V} from a given initial surface $\mathbf{s}(0) = \Gamma$. Instead of solving a time-dependent problem for $\mathbf{s}(t)$, the fast marching method solves for a function $\zeta(\mathbf{x})$ which represents the time it takes for the surface to reach \mathbf{x} . By the definition of ζ , we have

$$\zeta(\mathbf{s}(t)) = t, \quad (\text{E.1})$$

with $\zeta = 0$ on Γ . Differentiating (E.1) with respect to t , and noting that $\nabla \zeta$ is normal to the surface, we arrive at the following boundary value problem

$$|\nabla \zeta| V = 1, \quad \zeta = 0 \text{ on } \Gamma, \quad (\text{E.2})$$

commonly referred to as the Eikonal equation.

Next, we describe the algorithm to solve (E.2) on a two-dimensional grid. In order to compute $|\nabla \zeta|$, an operator D_{ij}^{-x} , representing the standard backward finite difference operation on the grid point ij , is defined as

$$D_{ij}^{-x} \zeta = \frac{\zeta_{ij} - \zeta_{(i-1)j}}{\Delta x}. \quad (\text{E.3})$$

Similarly, D^{+x} , D^{-y} , and D^{+y} denote forward in x , backward and forward in y finite difference operators respectively. To guarantee a unique viscosity solution¹⁹ of the evolving surface, one should consider an upwind finite difference scheme to compute the gradient, which is

¹⁹See Sethian (1996) on the reason behind seeking a viscosity solution.

conveniently written as

$$\begin{aligned} |\nabla\zeta| &\approx [(\max(D_{ij}^{-x}\zeta, 0)^2 + \min(D^{+x}\zeta_{ij}, 0)^2 + (\max(D_{ij}^{-y}\zeta, 0)^2 + \min(D^{+y}\zeta_{ij}, 0)^2)]^{1/2} \\ &= [(\max(D_{ij}^{-x}\zeta, 0)^2 + \max(-D^{+x}\zeta_{ij}, 0)^2 + (\max(D_{ij}^{-y}\zeta, 0)^2 + \max(-D^{+y}\zeta_{ij}, 0)^2)]^{1/2}. \end{aligned} \quad (\text{E.4})$$

Using (E.4), we rewrite (E.2) in an algebraic form

$$[(\max(D_{ij}^{-x}\zeta, D^{+x}\zeta_{ij}, 0)^2 + (\max(D_{ij}^{-y}\zeta, -D^{+y}\zeta_{ij}, 0)^2)]^{1/2} = \frac{1}{V(x, y)}. \quad (\text{E.5})$$

Note that if the neighboring values of ζ_{ij} are known, then (E.5) is a quadratic equation for ζ_{ij} that can be solved analytically.

The fast marching method begins with the following initialization step

1. Assign $\zeta(x) = 0$ for grid points in the area enclosed by the initial surface, and tag them as *accepted*.
2. Assign $\zeta(x) = +\infty$ for the remaining grid points, and tag them as *far*.
3. Among the *accepted* points, identify the points that are in the neighborhood of points tagged as *far*, and tag them as *considered*.

The key step in the fast marching method is to update ζ with a trial value using (E.5) for grid points tagged as *considered*, but only accept the update with the smallest value. In order to identify the smallest value efficiently, the grid points tagged as *considered* are stored in a min-heap²⁰ structure (Sedgewick and Wayne, 2008) borrowed from discrete network algorithms. The fast marching method then proceeds as follows.

1. Construct a min-heap structure for the *considered* points.
2. Access the root (minimum value) of the heap.
3. Find a trial solution $\tilde{\zeta}$ on the neighbors of the root using (E.5). If the trial solution is smaller than the present values, then update $\zeta(x) = \tilde{\zeta}$.
4. If a point, previously tagged as *far*, is updated using a trial value, relabel it as *considered*, and add it to the heap structure.
5. Tag the root of the heap as *accepted*, and delete it from the heap.
6. Repeat steps 2 to 5, until every grid point is tagged as *accepted*.

Fig. E.20 demonstrates the fast marching method used to track an initial surface

$$(9x^2 - 1)^2 - (3y + 1)(1 - 3y)^3 = 0, \quad (\text{E.6})$$

growing with a uniform outward normal velocity $V(x) = 1$.

²⁰A min-heap structure is a complete binary tree with a property that the value at any given node is less than or equal to the values at its children.

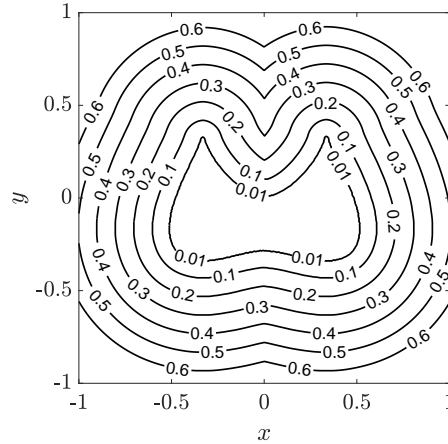


Figure E.20: The level sets of the solution to the Eikonal equation (E.2), computed using the fast marching method, describe a surface evolving with outward normal velocity $V(x, y) = 1$.

References

References

- N. C. Admal, G. Po, J. Marian, A unified framework for polycrystal plasticity with grain boundary evolution, *International Journal of Plasticity* 106 (2018) 1–30.
- R. Kobayashi, J. A. Warren, W. C. Carter, Vector-valued phase field model for crystallization and grain boundary formation, *Physica D: Nonlinear Phenomena* 119 (1998) 415–423.
- R. Kobayashi, J. A. Warren, W. C. Carter, A continuum model of grain boundaries, *Physica D: Nonlinear Phenomena* 140 (2000) 141–150.
- B. Runnels, I. J. Beyerlein, S. Conti, M. Ortiz, An analytical model of interfacial energy based on a lattice-matching interatomic energy, *Journal of Mechanics and Physics of Solids* 89 (2016a) 174–193.
- B. Runnels, I. J. Beyerlein, S. Conti, M. Ortiz, A relaxation method for the energy and morphology of grain boundaries and interfaces, *Journal of Mechanics and Physics of Solids* 94 (2016b) 388–408.
- T. Watanabe, Grain boundary engineering: historical perspective and future prospects, *Journal of Material Science* 46 (2011) 4095–4115.
- W. W. Mullins, Two-dimensional motion of idealized grain boundaries, *Journal of Applied Physics* 27 (1956) 900–904.
- K. Chen, J. Han, X. Pan, D. J. Srolovitz, The grain boundary mobility tensor, *Proceedings of the National Academy of Sciences of the United States of America* 117 (2020) 4533–4538.
- D. L. Olmsted, S. M. Foiles, E. A. Holm, Survey of computed grain boundary properties in face-centered cubic metals: I. grain boundary energy, *Acta Materialia* 57 (2009) 3694–3703.

- V. V. Bulatov, B. W. Reed, M. Kumar, Anisotropy of interfacial energy in five dimensions, arXiv: Material Science (2013).
- A. Rollett, One crystal out of many, *Science* 362 (2018) 996–998.
- K. Barmak, E. Eggeling, D. Kinderlehrer, R. Sharp, S. Ta’asan, A. D. Rollett, K. R. Coffey, Grain growth and the puzzle of its stagnation in thin films: The curious tale of a tail and an ear, *Progress in Materials Science* (2013) 987–1055.
- M. Upmanyu, R. W. Smith, D. J. Srolovitz, Atomicistic simulation of curvature driven grain boundary migration, *Interface Science* 6 (1998) 41–58.
- K. G. F. Janssens, D. Olmsted, E. A. Holm, S. M. Foiles, S. J. Plimton, P. M. Derlet, Computing the mobility of grain boundaries, *Nature Materials* 5 (2006) 124–127.
- M. P. Anderson, D. J. Srolovitz, G. S. Grest, P. S. Sahni, Computer simulation of grain growth I, *Acta Metallurgica* 32 (1958) 783–791.
- M. P. Anderson, G. S. Grest, D. J. Srolovitz, Computer simulation of grain growth in three dimensions, *Philosophical Magazine B* 59 (1989) 293–329.
- M. I. Mendeleev, D. J. Srolovitz, Co-segregation effects on boundary migration, *Interface Science* 10 (2002) 191–199.
- M. Upmanyu, G. N. Hassold, A. Kazaryan, E. A. Holm, Y. Wang, B. Patton, D. J. Srolovitz, Boundary mobility and energy anisotropy effects on microstructural evolution during grain growth, *Interface Science* 10 (2002) 201–216.
- Z. Yang, S. Sista, J. W. Elmer, T. DebRoy, Three dimensional Monte carlo simulation of grain growth during GTA welding of titanium, *Acta Materialia* 48 (2000) 4813–4825.
- M. Hillert, On the theory of normal and abnormal grain growth, *Acta Metallurgica* 13 (1965) 227–238.
- S. M. Allen, J. W. Cahn, A microscopic theory for antiphase boundary motion and its application to antiphase domain coarsening, *Acta Metallurgica* 27 (1979) 1085–1095.
- H. J. Frost, C. V. Thompson, D. T. Walton, Simulation of thin film grain structures—I. grain growth stagnation, *Acta Metallurgica et Materialia* 38 (1990) 1455–1462.
- H. J. Frost, C. V. Thompson, C. L. Howe, J. Whang, A two dimensional computer simulation of capillarity-driven grain growth: Preliminary results, *Scripta Metallurgica* 22 (1988) 65–70.
- D. Kinderlehrer, J. H. Lee, I. Livshits, A. D. Rollett, S. Ta’asan, Mesoscale simulation of grain growth, *Materials Science Forum* 467–470 (2004).
- D. Kinderlehrer, I. Livshits, S. Ta’asan, A variational approach to modeling and simulation of grain growth, *SIAM Journal on Scientific Computing* 28 (2006) 1694–1715.

- H.-K. Zhao, T. Chan, B. Merriman, S. Osher, A variational level set approach to multiphase motion, *Journal of Computational Physics* 127 (1996) 179–195.
- J. Fausty, N. Bozzolo, D. P. Munoz, M. Bernacki, A novel level-set finite element formulation for grain growth with heterogeneous grain boundary energies, *Materials & Design* 160 (2018) 578–590.
- B. Merriman, J. K. Bence, S. J. Osher, Diffusion generated motion by mean curvature, *Proceedings of the Computational Crystal Growers Workshop* (1992) 72–83.
- S. Esedoğlu, F. Otto, Threshold dynamics for networks with arbitrary surface tensions, *Communications on Pure and Applied Mathematics* 68 (2015) 808–864.
- M. Elsey, S. Esedoğlu, P. Smereka, Diffusion generated motion for grain growth in two and three dimensions, *Journal of Computational Physics* 228 (2009) 8015–8033.
- M. Elsey, S. Esedoğlu, P. Smereka, Large scale simulations and parameter study for a simple recrystallization model, *Philosophical Magazine* 91 (2011) 1607–1642.
- A. Zaitzeff, S. Esedoğlu, K. Garikipati, Second order threshold dynamics schemes for two phase motion by mean curvature, *Journal of Computational Physics* 410 (2020) 109404.
- A. Basak, A. Gupta, A two-dimensional study of coupled grain boundary motion using the level set method, *Modelling and Simulation in Materials Science and Engineering* 22 (2014).
- H. Hallberg, V. V. Bulatov, Modeling of grain growth under fully anisotropic grain boundary energy, *Modelling and Simulation in Materials Science and Engineering* 27 (2019) 045002.
- T. Joshi, R. Arora, A. Basak, A. Gupta, Equilibrium shape of misfitting precipitates with anisotropic elasticity and anisotropic interfacial energy, *Modelling and Simulation in Materials Science and Engineering* 28 (2020).
- A. M. Jokisaari, P. W. Voorhees, J. E. Guyer, J. Warren, O. G. Heinonen, Benchmark problems for numerical implementations of phase field models, *Computational Materials Science* 126 (2017) 139–151.
- L.-Q. Chen, Phase-field models for microstructure evolution, *Annual Review of Materials Research* 32 (2002) 113–140.
- T. Hirouchi, T. Tsuru, Y. Shibutani, Grain growth prediction with inclination dependence of [110] tilt grain boundary using multi-phase-field model with penalty for multiple junctions, *Computational Materials Science* 53 (2012) 474–482.
- I. Steinbach, Phase-field models in materials science, *Modelling and Simulation in Materials Science and Engineering* 17 (2009) 073001.
- J. A. Warren, R. Kobayashi, A. E. Lobkovsky, W. C. Carter, Extending phase field models of solidification to polycrystalline materials, *Acta Materialia* 51 (2003) 6035–6058.

- D. Fan, S. P. Chen, L.-Q. Chen, P. W. Voorhees, Phase-field simulation of 2-D ostwald ripening in the highvolume fraction regime, *Acta Materialia* 50 (2002).
- C. J. Permann, M. R. Tonks, B. Fromm, D. R. Gaston, Order parameter re-mapping algorithm for 3D phase field model of grain growth using fem, *Computational Materials Science* 115 (2016).
- J. G. Ribot, V. Agrawal, B. Runnels, A new approach for phase field modeling of grain boundaries with strongly nonconvex energy, *Modelling and Simulation in Materials Science and Engineering* 27 (2019).
- N. Moelans, B. Blanpain, P. Wollants, Quantitative phase-field approach for simulating grain growth in anisotropic systems with arbitrary inclination and misorientation dependence, *Physical Review Letters* 101 (2008) 025502.
- H.-K. Kim, S. G. Kim, W. Dong, I. Steinbach, B.-J. Lee, Phase-field modeling for 3d grain growth based on a grain boundary energy database, *Modelling and Simulation in Materials Science and Engineering* 22 (2014) 034004.
- W. T. Read, W. Shockley, Dislocation models of crystal grain boundaries, *Physical Review* 78 (1950) 275.
- E. A. Holm, D. L. Olmsted, S. M. Foiles, Comparing grain boundary energies in face-centered cubic metals: Al, Au, Cu and Ni, *Scripta Materialia* 63 (2010) 905–908.
- V. V. Bulatov, B. W. Reed, M. Kumar, Grain boundary energy function for fcc metals, *Acta Materialia* 65 (2014) 161–175.
- D. Wolf, Structure-energy correlation for grain boundaries in fcc metals—III. Symmetrical tilt boundaries, *Acta Metallurgica et Materialia* 38 (1990) 781–790.
- J. K. Mason, S. Patala, Basis functions on the grain boundary space: Theory, arXiv preprint arXiv:1909.11838 (2019).
- H.-K. Kim, S. G. Kim, W. Dong, I. Steinbach, B.-J. Lee, Phase-field modeling for 3D grain growth based on a grain boundary energy database, *Modelling and Simulation in Materials Science and Engineering* 22 (2014) 034004.
- R. Alicandro, A. Braides, J. M. Shah, Free-discontinuity problems via functionals involving the L1-norm of the gradient and their approximations, *Interface and Free Boundaries* 1 (1999) 17–37.
- A. E. Lobkovsky, J. A. Warren, Sharp interface limit of a phase-field model of crystal grains, *Physical Review E* 63 (2001) 051605.
- M. R. Dorr, J.-L. Fattebert, M. E. Wickett, J. F. Belak, P. E. A. Turchi, A numerical algorithm for the solution of a phase-field model of polycrystalline materials, *Journal of Computational Physics* 229 (2010) 626–641.

- N. C. Admal, J. Segurado, J. Marian, A three-dimensional misorientation axis- and inclination-dependent Kobayashi–Warren–Carter grain boundary model, *Journal of the Mechanics and Physics of Solids* 128 (2019) 32–53.
- M. Jacobs, F. Leger, W. Li, S. Osher, Solving large-scale optimization problems with a convergence rate independent of grid size, *SIAM Journal on Numerical Analysis* 57 (2019) 1100–1123.
- T. Salvador, S. Esedoğlu, The role of surface tension and mobility model in simulations of grain growth, arXiv:1907.11574 (2019).
- G. Martine La Boissonière, R. Choksi, K. Barnak, S. Esedoğlu, Statistics of grain growth: Experiment versus the phase-field-crystal and mullins models, *Materialia* 6 (2019) 100280.
- J. N. Tsitsiklis, Efficient algorithms for globally optimal trajectories, *IEEE Transactions on Automatic Control* 40 (1995) 1528–1538.
- C. Herring, *Surface Tension as a Motivation for Sintering*, McGraw Hill, 1951. doi:[10.1007/978-3-642-59938-5_2](https://doi.org/10.1007/978-3-642-59938-5_2).
- S. Esedoğlu, S. Ruuth, R. Tsai, Diffusion generated motion using signed distance functions, *Journal of Computational Physics* 229 (2010) 1017–1042.
- J. von Neumann, *Metal Interfaces*, American Society for Metals, Cleveland, 1952.
- M. S. Alnaes, J. Blechta, J. Hake, A. Johansson, B. Kehlet, A. Logg, C. Richardson, J. Ring, M. E. Rognes, G. N. Wells, The FEniCS Project Version 1.5, *Archive of Numerical Software* 3 (2015).
- Y. Saad, M. H. Schultz, GMRES: A generalized minimal residual algorithm for solving nonsymmetric linear systems, *SIAM Journal on Scientific Computing* 7 (1986) 856–869.
- R. Li, Y. Saad, GPU-accelerated preconditioned iterative linear solvers, *The Journal of Supercomputing* 63 (2013) 443–466.
- N. K. Govindaraju, B. . Lloyd, Y. Dotsenko, B. Smith, J. Manferdelli, High performance discrete fourier transforms on graphics processors, *Proceedings of the 2008 ACM/IEEE Conference on Supercomputing* (2008).
- J. C. Li, Possibility of subgrain rotation during recrystallization, *Journal of Applied Physics* 33 (1962) 2958–2965.
- S. Thomas, K. Chen, J. Han, P. K. Purohit, D. J. Srolovitz, Reconciling grain growth and shear-coupled grain boundary migration, *Nature communications* 8 (2017) 1–12.
- C. Wei, L. Zhang, J. Han, D. J. Srolovitz, Y. Xiang, Grain boundary triple junction dynamics: a continuum disconnection model, *SIAM Journal on Applied Mathematics* 80 (2020) 1101–1122.

- B. Runnels, V. Agrawal, Phase field disconnections: A continuum method for disconnection-mediated grain boundary motion, *Scripta Materialia* 186 (2020) 6–10.
- H. Miura, M. Kato, T. Mori, Temperature dependence of the energy of Cu [110] symmetrical tilt grain boundaries, *Journal of Material Science Letters* 13 (1994) 46–48.
- M. J. D. Powell, Algorithms for nonlinear constraints that use lagrangian functions, *Mathematical Programming* 14 (1978) 224–248.
- H. W. Kuhn, The hungarian method for the assignment problem, *Naval Research Logistics Quarterly* 2 (1955) 83–97.
- N. Komodakis, J. Pesquet, Playing with duality: An overview of recent Primal-dual approaches for solving large-scale optimization problems, *IEEE Signal Processing Magazine* 32 (2015) 31–54.
- D. L. Donoho, Compressed sensing, *IEEE Transactions on Information Theory* 52 (2006) 1289–1306.
- A. Chambolle, T. Pock, A first-order primal-dual algorithm for convex problems with applications to imaging, *Journal of Mathematical Imaging and Vision* 40 (2011) 120–145.
- S. Shalev-Shwartz, Y. Singer, A primal-dual perspective of online learning algorithms, *Machine Learning* 69 (2007) 115–142.
- P. L. Combettes, J.-C. Pesquet, Proximal Splitting Methods in Signal Processing, volume 49 of *Springer Optimization and Its Applications*, Springer, New York, 2011. doi:[10.1007/978-1-4419-9569-8_10](https://doi.org/10.1007/978-1-4419-9569-8_10).
- J. Sethian, A fast marching level set method for monotonically advancing fronts, *Proceedings of the National Academy of Sciences of the United States of America* 93 (1996) 1591–1595.
- R. Sedgewick, K. Wayne, *Algorithms*, Addison-Wesley, 2008.